



ORIGINAL RESEARCH ARTICLE

Scanning Strategy of Multi-Layer and Multi-Track Laser Cladding for Radial Grooves of Annular Thin-walled Parts

Lei Wang, Xianwang Wu, Tong Wang, Zelin Zhang, Xianzhi Jin, Xuhui Xia, and Yubo Liu

Submitted: 30 June 2023 / Revised: 29 October 2023 / Accepted: 26 November 2023

To improve the forming quality, twelve annular cross-scanning strategy models for radial groove laser cladding of annular thin-walled parts are established in the paper. A thermo-mechanical coupling simulation is carried out to investigate the temperature, stress and deformation under different scanning strategies. Based on the results of various scanning strategies, the scanning strategy with the minimum deformation is obtained. The single-layer and single-track results indicate that the maximum value of residual stress is at the junction of cladding layer and the groove. For the single-layer and multi-track, the scanning strategy of cold overlapping between tracks is better than that of hot overlapping between tracks. For the multi-layer and single-track, the scanning strategy of hot overlapping between layers is better than that of cold overlapping between layers. Among the twelve scanning strategies, the scanning strategy with the minimum heat accumulation has the minimum deformation for the two-layer and two-track. The optimal scanning strategy is the cold overlapping between tracks first and then the hot overlapping between layers. Finally, the laser cladding experiment is carried out on radial grooves of annular thin-walled parts with the optimal scanning strategy, and the simulation results are verified.

Keywords annular thin-walled parts, laser cladding, radial grooves, scanning strategy, thermo-mechanical coupling

1. Introduction

As an advanced forming technology with high efficiency, low pollution and low cost and high flexibility, laser cladding can rapidly manufacture or repair complex mechanical parts (Ref 1). It is widely gaining the attention of high-tech industries such as the automotive, aerospace, and biomedical (Ref 2). In these industries, many large functional components such as aero-engine blades and combustion chambers have annular cross section inclined parts (Ref 3). The parts are called the

thin-walled parts because the ratio of thickness to inner diameter or outline size is generally less than 1:20. It has the advantages of compact structure, strong bearing capacity and lightweight (Ref 4). Therefore, the study of laser cladding for annular parts is of great significance to practical laser processing.

Some scholars have carried out the following research on annular parts. For example, Cui et al. analyzed the thermal stress evolution and residual stress distribution of multi-track multi-layer on a partial shaft part by LMD. The results showed that the arc copying lap scanning method had a relatively smaller maximum thermal stress and residual stress after cooling than the axial parallel lap scanning method (Ref 5). Lian et al. investigated the influence of laser power, scanning speed, gas flow and other factors on clad width, clad height, and dilution rate in annular surface laser cladding with curved path. They used central composite designs to develop mathematical models. The models optimized these factors to improve the geometric characteristics of the clad and the predicted accuracy was verified (Ref 6). Shu et al. analyzed the thermo-mechanical coupling problem adopting a numerical approach during the wear annular surface laser cladding. The residual stress of the simulation was in good agreement with experimentally obtained results. The results had a guiding significance to process optimization of the annular surface laser cladding (Ref 7).

In various annular thin-walled parts, there may be single or multiple radial or axial grooves in the middle of the thin-walled strip. The grooves generate friction heat because the actual contact pressure is usually greater than the pressure during smooth contact. The friction heat enlarges the surface damage area of parts and ultimately reduces the service life (Ref 8). Therefore, the application for laser cladding of annular thin-walled parts with the radial grooves can effectively improve the quality and service life. Compared to laser cladding of flat

Lei Wang, Xianwang Wu, and Tong Wang, Key Laboratory of Metallurgical Equipment and Control Technology, Ministry of Education, Wuhan University of Science and Technology, Wuhan, China; and Hubei Key Laboratory of Mechanical Transmission and Manufacturing Engineering, Wuhan University of Science and Technology, Wuhan, China; **Zelin Zhang and Xianzhi Jin**, Key Laboratory of Metallurgical Equipment and Control Technology, Ministry of Education, Wuhan University of Science and Technology, Wuhan, China; and Precision Manufacturing Institute, Wuhan University of Science and Technology, Wuhan, China; **Xuhui Xia**, Key Laboratory of Metallurgical Equipment and Control Technology, Ministry of Education, Wuhan University of Science and Technology, Wuhan, China; Hubei Key Laboratory of Mechanical Transmission and Manufacturing Engineering, Wuhan University of Science and Technology, Wuhan, China; and Precision Manufacturing Institute, Wuhan University of Science and Technology, Wuhan, China; and **Yubo Liu**, Xiangyang Boya Precision Industrial Equipments Co.,Ltd, Xiangyang, China. Contact e-mail: wangtong@wust.edu.cn.

parts, non-flat surfaces are more challenging to uniformly distribute laser energy and powder (Ref 9). Therefore, it is difficult to carry out laser cladding on thin-walled parts with grooves.

In view of the forming quality problems related to groove laser cladding, several studies have been conducted. Weng et al. successfully repaired V-grooves on ductile cast iron substrates using diode laser cladding technology with Fe-based self-fluxing alloy powder as the cladding material. The repaired samples were free of any defects such as pores and cracks (Ref 10). Feng et al. proposed a novel test method to evaluate the crack resistance by laser cladding based on the crack rate as the evaluation metric. By controlling the depth/width of the Y-groove, the method can effectively reflect the crack rate and prepare the high hardness crack-free coatings (Ref 11). Wang et al. studied laser cladding on 1045 steel substrates with isosceles trapezoidal grooved-textures using Fe-based powder. The results showed that there was complex tendencies of the toughness and strength of the specimen with an increase in groove depth (Ref 12). In a word, many literatures have the contribution to the laser cladding for grooves, but the cladding objects in the literatures are flat parts. The grooves of non-flat parts (such as annular parts) which are more difficult to form are selected as the research object of laser cladding in few literatures. There are two kinds of annular grooves: axial and radial. An axial groove is parallel to the central axis of an annular part, and the length does not exceed the width. However, the surface area of a radial groove around an annular part is generally larger and the degree of non-flat is higher. Consequently, a poorly forming cladding layer on a radial groove can be easily obtained more than a uniformly forming cladding layer.

For the problem of poor forming quality, some previous investigations indicate that scanning strategy process can be used to improve the quality of laser cladding because a reasonable scanning strategy process can reduce the residual stress and deformation in the cladding part (Ref 13). For instance, Niu et al. designed scanning strategies of selective laser melting by changing rotation angle between scanning tracks. The results showed that the scanning strategies had a limited impact on the relative density of samples while influencing the hardness of the samples (Ref 14). Zhao et al. employed laser cladding technology to fabricate 24CrNiMo alloy steel samples additively. Their study demonstrated that the microstructural evolution, texture, and mechanical properties of the deposited samples were influenced by varying inter-layer time intervals and scanning strategies between deposited layers (Ref 15). Patra et al. assessed the bond strength of laser clad stellite 21 layers deposited on AISI H13 tool steel under various scanning strategies and linear energy. They concluded that the laser tracks in the shear load direction exhibited higher strength compared to those in the transverse direction (Ref 16). Li et al. also examined the effects of different scanning strategies on the residual stress and deformation of hollow-ring laser cladding. It was ultimately determined that the appropriate scanning pattern could effectively reduce residual stress and mitigate substrate deformation (Ref 17). Sun et al. analyzed the building accuracy of generating thin-walled cylinders via employing scanning strategy, laser power adjustment and helical scanning optimization. Finally, it was verified that the result of the method which combined synclastic scanning strategy, reversed scanning strategy, and new collative variable of Z-axis increment with these optimal tactics had fewer defects and better performance (Ref 18).

The above research primarily concentrates on the numerical simulation and experimentation of laser cladding processes for flat parts with various materials and shapes, aiming to produce high-quality cladding layers through scanning strategy technology. However, there is a scarcity of research exploring the scanning strategy of laser cladding with the minimal deformation for radial grooves of annular thin-walled parts. To explore the impact of scanning strategy on forming quality, this paper establishes a model for multi-layer and multi-track (with a two-layer and two-track example) laser cladding. A range of annular cross-scanning strategy models is designed to investigate the temperature, stress, and deformation during the laser cladding process. The temperature field, stress field and deformation of single-layer and single-track, single-layer and multi-track, multi-layer and single-track and multi-layer and multi-track configurations are obtained using a thermo-mechanical coupling numerical simulation method. By comparing the results of various scanning strategies, the scanning strategy with the least deformation is selected and verified by experiments. The results can offer valuable scientific and theoretical guidance for the practical selection of scanning strategies in multi-layer and multi-track laser cladding applications.

2. Scanning Strategy Model and Simulation Method

2.1 Radial Grooves Model

Taking an annular thin-walled part as an example, the inner diameter is d_i , the thickness is w_B and the width is w_L . The number of radial grooves is t_i on the outer surface of the part and the depth of each groove is H and the width is b . The model is as shown in Fig. 1. The distance between the grooves is d , and the number of cladding layers on each groove is l_j . The cladding thickness of each layer is h and the cross-sectional diagram is shown in Fig. 2.

In actual additive manufacturing processes, surface coating strengthening or surface repair remanufacturing technology of parts often designs a certain machining allowance for the thickness of the cladding layer. It means that the large-area surface cladding layer needs a comprehensive approach involving multi-layer and multi-track cladding forming (Ref 19). If the groove depth (H) is greater than the maximum single-layer cladding thickness (h_m), a multi-layer cladding method is adopted for meeting the machining allowance. The total thickness of the cladding layer will not be less than the groove depth after using the method. Consequently, cladding thickness (h) and the number of cladding layers (l_j) are designed based on the groove depth (H). The relationship is depicted in Table 1.

2.2 Scanning Strategy

A reasonable and continuous scanning strategy can effectively improve the concentration of laser heat source and reduce the residual stress in the cladding layer (Ref 20). The scanning strategy is the spatial moving pattern of the laser beam. For a single-layer scan, the scanning strategy varies with different scanning direction, scanning sequence, scanning vector rotation angle and other parameters. In the selection of scanning strategy, the scanning direction and scanning sequence relative

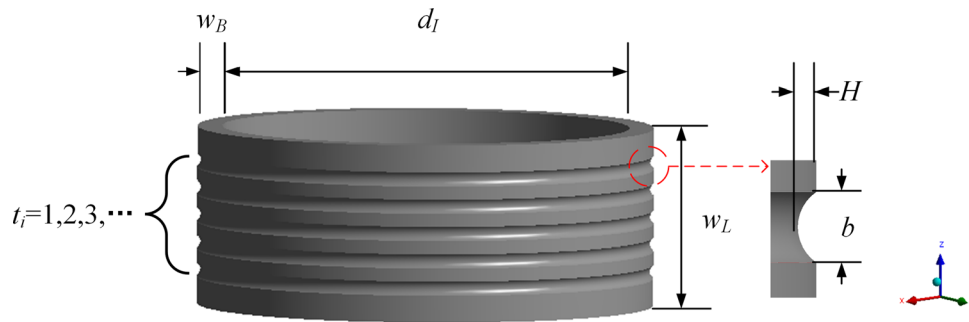


Fig. 1 Radial grooves on annular thin-walled parts

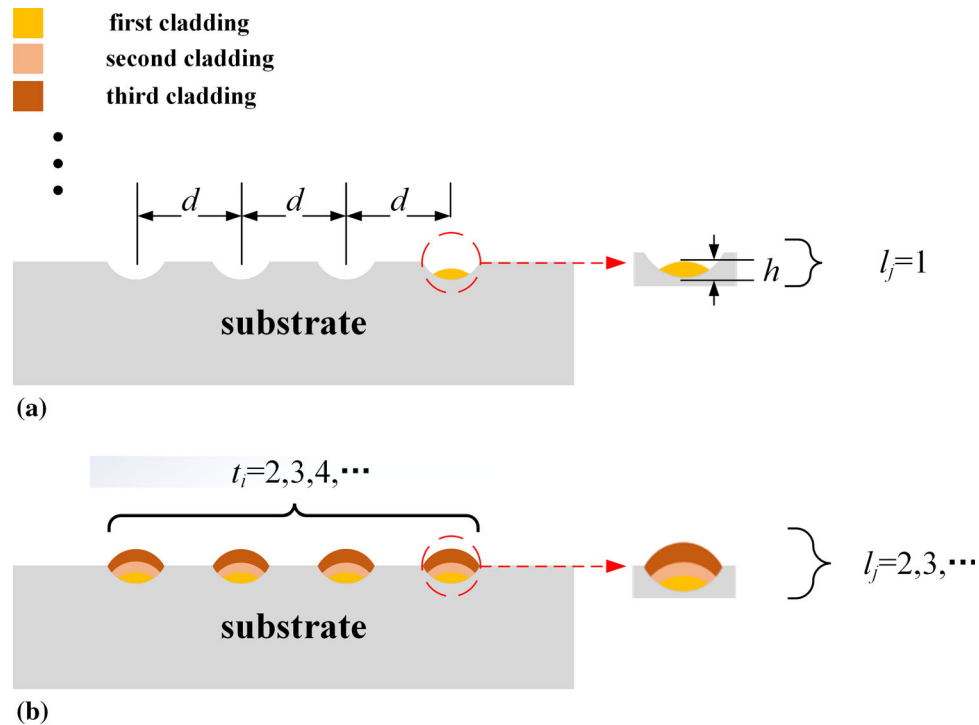


Fig. 2 Cross-sectional diagram of single-layer and single-track (a) and multi-layer and multi-track (b) radial grooves on annular thin-walled parts

Table 1 The laser cladding parameters

Cladding parameters				...
Groove depth, H , mm	$0 < H \leq h_m$	$h_m < H \leq 2h_m$	$2h_m < H \leq 3h_m$...
Cladding thickness, h (mm)	$0 < h \leq h_m$	$0 < 2h \leq 2h_m$	$0 < 3h \leq 3h_m$...
Cladding layer, l_j	$l_j \geq 1$	$l_j \geq 2$	$l_j \geq 3$...

to the geometric shape are used to improve the uniformity of temperature distribution (Ref 21). Considering the present situation, the scanning sequence of most laser heat source paths is often in a continuous simple mode such as scanning in the same or opposite direction (Ref 22). Therefore, this paper optimizes a continuous and orderly scanning sequence on the grooves. Specifically, the starting point of each path is always scanned from the groove on the outermost end of the annular thin-walled parts (referred to as the first side). Additionally, the

starting point of each layer moves continuously as much as possible. To ensure the completion of all cladding layers on a single groove first, the scanning sequence starts with the laser cladding from one end of the thin-walled part's groove. The laser heat source then proceeds to the adjacent ground groove to continue cladding until the last groove (called the last side). This scanning sequence is referred to as tracks first, then layers (referred to as S1). On the other hand, to ensure the completion of a cladding layer on all grooves first, the scanning sequence

starts by coating a cladding layer from one end of the thin-walled part's groove. The laser heat source then directly turns toward the adjacent ground groove to scan the next cladding layer until it reaches the final groove. When the laser prepares for scanning the next layer, there are two scanning sequences. Firstly, the laser still initiates from the original groove and this sequence is referred to as layers first, then tracks on the first side (referred to as S2). Additionally, the laser continues cladding directly from the final groove and is referred to as layers first, then tracks on the last side (referred to as S3), as shown in Fig. 3.

The laser heat source scans the radial grooves in two directions: clockwise and counterclockwise. In this paper, the negative z axis is taken as the overlooking angle. The counterclockwise direction is positive (referred to as PD) and the clockwise direction is negative (referred to as ND). The end position of each laser scanning path is the starting point because the path is annular, so the point is called the starting and ending point as shown in Fig. 4.

There are mainly two kinds of scanning paths for single-layer laser cladding on annular parts. According to the expression of path length and cooling time, the same direction process of adjacent scanning paths is called hot overlapping while the reverse process is cold overlapping (Ref 23). In the case of single-layer and multi-track, there are two overlapping strategies for the radial grooves between tracks. One of them is that the scanning paths of every cladding layer adjacent to each other in

the same layer are all in the same direction. The strategy is hot overlapping between tracks (referred to as HT). Another situation is that the scanning paths adjacent to each other in the same layer are all in the reverse direction. The strategy is cold overlapping between tracks (referred to as CT). In the case of multi-layer and single-track, there are two overlapping

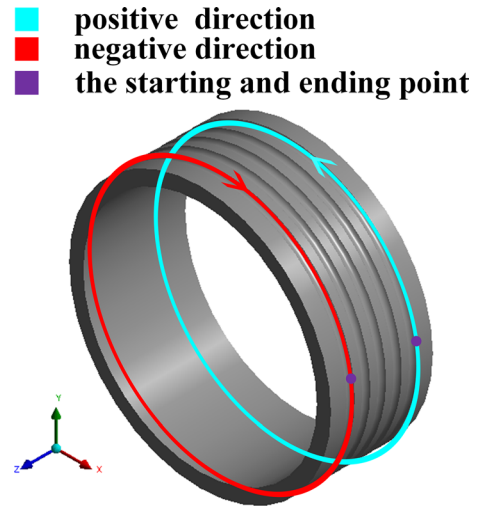


Fig. 4 positive direction and negative direction

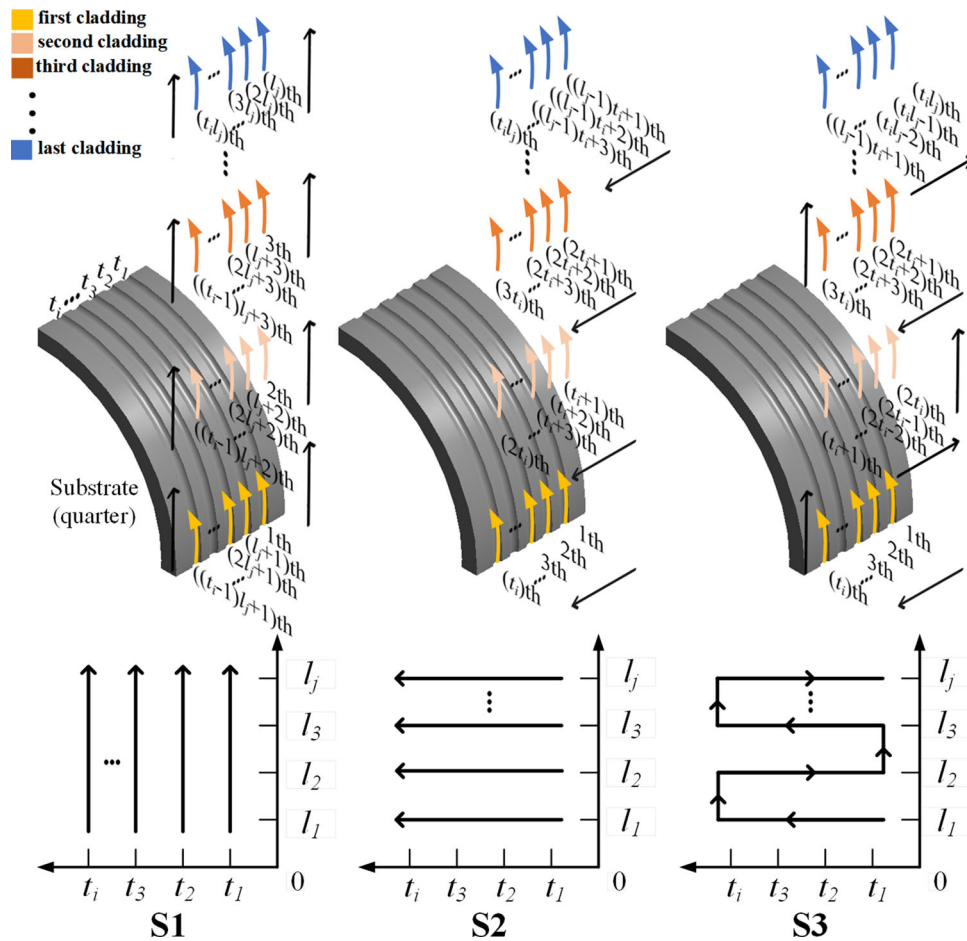


Fig. 3 Diagram of scanning sequences

strategies for the radial grooves between layers. One strategy is that the scanning paths of every cladding layer adjacent to each other in the same track are all in the same direction. The strategy is hot overlapping between layers (referred to as HL). Another situation is that the scanning paths adjacent to each other in the same track are all in the reverse direction. The strategy is called cold overlapping between layers (referred to as CL).

In the case of multi-layer and multi-track laser cladding, a comparison is made between annular parts created using overlapping strategies in single-layer and multi-track and multi-layer and single-track configurations. Four different overlapping strategies have been identified. The first strategy involves the scanning paths of every cladding layer adjacent to each other in every layer and track being all in the same direction (referred to as HT-HL). The second strategy shows the scanning paths in every layer being in the same direction, but in every track being in the reverse direction (referred to as HT-CL). The third strategy involves scanning paths in every layer being in the reverse direction, but in every track being in the same direction (referred to as CT-HL). Finally, the fourth strategy shows the scanning paths in every layer and track being all in the reverse direction (referred to as CT-CL), as shown in Fig. 5.

To sum up, the scanning sequences and overlapping strategies do not change with the increase or decrease in the cladding layer number (l_j) and groove number (t_i). Therefore, there are always 12 scanning strategies based on them in multi-layer and multi-track in this paper.

2.3 Thermo-Mechanical Coupling Finite Element Simulation

The temperature field distribution of the interaction between the laser heat source and the material is numerically simulated using ANSYS simulation software. It is essential for the convergence of the calculation results to establish certain boundary conditions for the temperature field and stress field. Therefore, the physical model filled with cladding material is established using birth-and-death element technology. The heat loss of air convective heat transfer is defined by Newton's cooling law. The equation is calculated as (Ref 24)

$$h_c = h_0 + \beta k(T - T_0)(T^2 + T_0^2) \quad (\text{Eq 1})$$

where h_c is the convective heat transfer coefficient. h_0 is the value of h_c at room temperature. β is the radiation coefficient. k is Boltzmann constant. T_0 is the initial temperature of substrate and cladding material, which is 22 °C. The specified heat source is applied to the cladding layer and the heat source model is shown in Fig. 6.

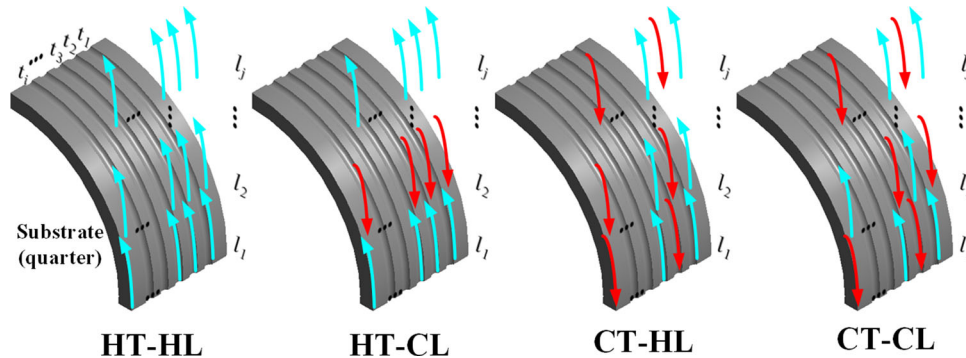


Fig. 5 Diagram of overlapping strategies in multi-layer and multi-track

The heat source equation is the basis of numerical simulation of temperature field. Appropriate heat source model can simplify calculation and improve the accuracy of numerical simulation (Ref 25). In the numerical simulation of temperature field, the laser energy acts on the substrate surface in the form of heat flux density, the radial light beam is exhibiting a Gaussian distribution and the light spot being rectangular. The heat source formula is calculated as (Ref 26)

$$q = Q \cdot \exp\left(-3 \frac{(X - d_o \cdot \cos(\frac{2\pi t}{n}))^2 + (Y - d_o \cdot \sin(\frac{2\pi t}{n}))^2 + Z^2}{BL}\right) \quad (\text{Eq 2})$$

$$Q = \frac{fP}{BL} \quad (\text{Eq 3})$$

where q is the specified heat source. Q is the maximum heat flux. X , Y and Z are, respectively, horizontal, vertical, and axial coordinates of the central point of the heat source on the surface of the laser cladding layer at a certain time. B and L are rectangular spot length and width. d_o is the outside diameter of annular thin-walled parts. t is a certain time. c is a single-track scanning period. f is energy conversion factor, $f \leq 1$. P is laser power.

Then, the thermal load obtained from transient thermal analysis is gradually applied to the mechanical model. The

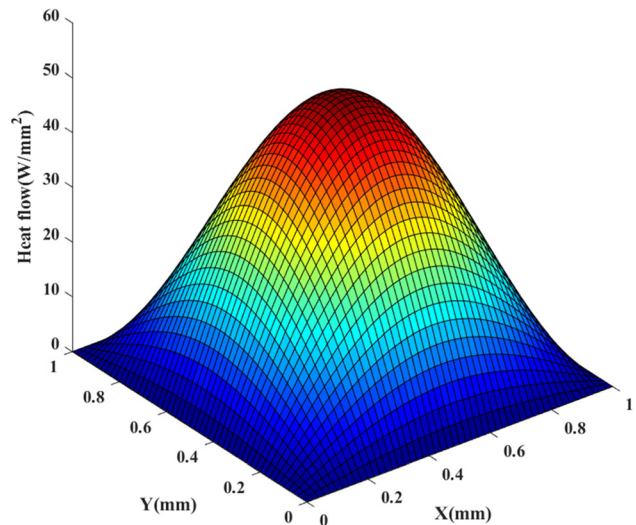


Fig. 6 Heat source model

transient mechanical analysis is carried out. The total strain produced by laser cladding can be expressed as (Ref 27)

$$\varepsilon = \varepsilon^{el} + \varepsilon^{th} + \varepsilon^{pl} \quad (\text{Eq 4})$$

where ε is the total strain, ε^{el} is elastic strain, ε^{th} is thermal strain and ε^{pl} is plastic strain. The initial conditions for thermal stress analysis can be set as (Ref 28)

$$\begin{cases} \{\sigma\} = 0t = 0 \\ \{\varepsilon\} = 0t = 0 \end{cases} \quad (\text{Eq 5})$$

where σ is the stress tensor. The detailed numerical simulation process about radial grooves of annular thin-walled parts established in this paper is shown in Fig. 7.

3. Case Application and Analysis

3.1 Parameter Condition

In this paper, the size parameters are based on thin-walled parts for inner ring seat of front and rear ring as the prototype case, which are set as shown in Table 2.

According to the optimization of the size parameters and Table 1, a two-layer and two-track configuration are selected in this paper. The selected scanning strategies are shown in Fig. 8, where the numbers indicate the scanning sequence, the number colors represent the number of cladding layers, and the arrows indicate the scanning direction.

The base material of annular thin-walled parts is ZG32MnMo and the powder material is 316L stainless steel. The material properties in the thermo-mechanical coupling analysis are obtained from the ANSYS software material library, as shown in Fig. 9. The chemical composition of 316L stainless steel powder is shown in Table 3.

316L stainless steel powder is spherical with particle size between 10-60 μm . The mean diameter, D10, D50, and D90 of the powder is provided in Table 4, where the D10, D50, and D90 represent the particle diameters at 10, 50, and 90% in cumulative distribution.

Proper combinations of some process parameters could control the cladding geometries and characteristics for high quality cladding layers (Ref 29). Therefore, the process parameters like laser power, scanning speed, powder feed rate and laser spot size are selected based on the current research and experimental equipment in this paper (Ref 30, 31). The values of the process parameters are shown in Table 5. A single factor experiment is carried out on the scanning strategy to measure the radial grooves deformation of annular thin-walled parts under different scanning strategies. Through the influence of scanning strategy technology on laser scanning paths, the substrate deformation results after cooling for a period are compared to determine the optimal scanning strategy process.

The validation experiment is based on the BS-ODE-6000-60-4H laser surface treatment equipment. The cladding test is

Table 2 The size parameters

Size parameters	Values
Inner diameter, d_i (mm)	149
Outside diameter, d_o (mm)	167
Thickness, w_B (mm)	9
Width, w_L (mm)	65
Groove spacing, d (mm)	16.5
Groove depth, H (mm)	2.5
Groove width, b (mm)	7
Cladding thickness, h (mm)	2.2
Number of grooves, t_i	2

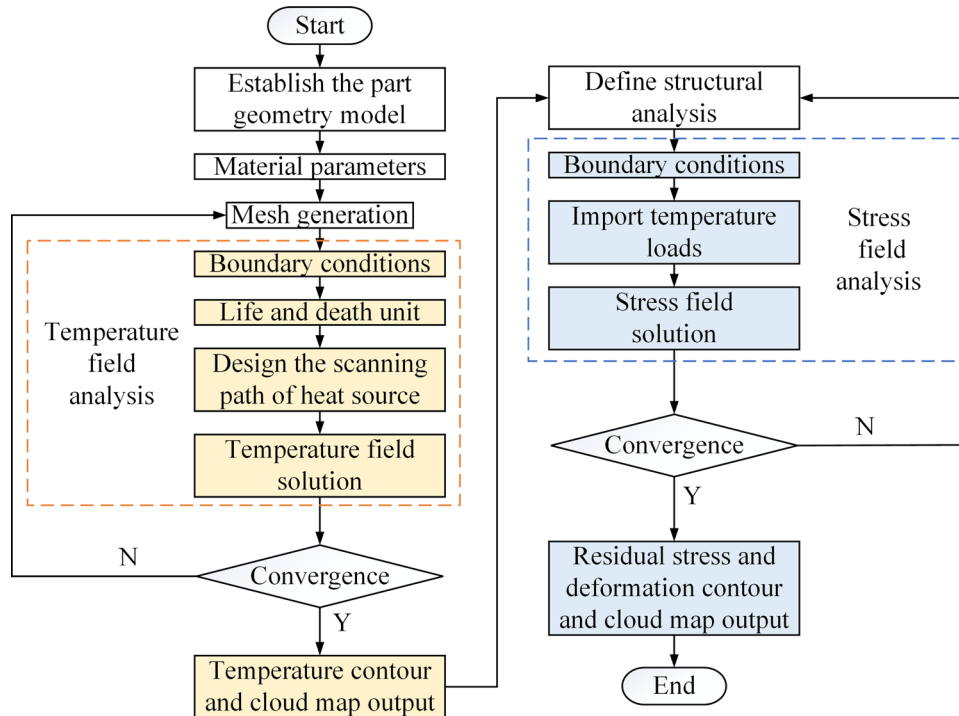


Fig. 7 Numerical simulation flowchart for radial grooves of annular thin-walled parts

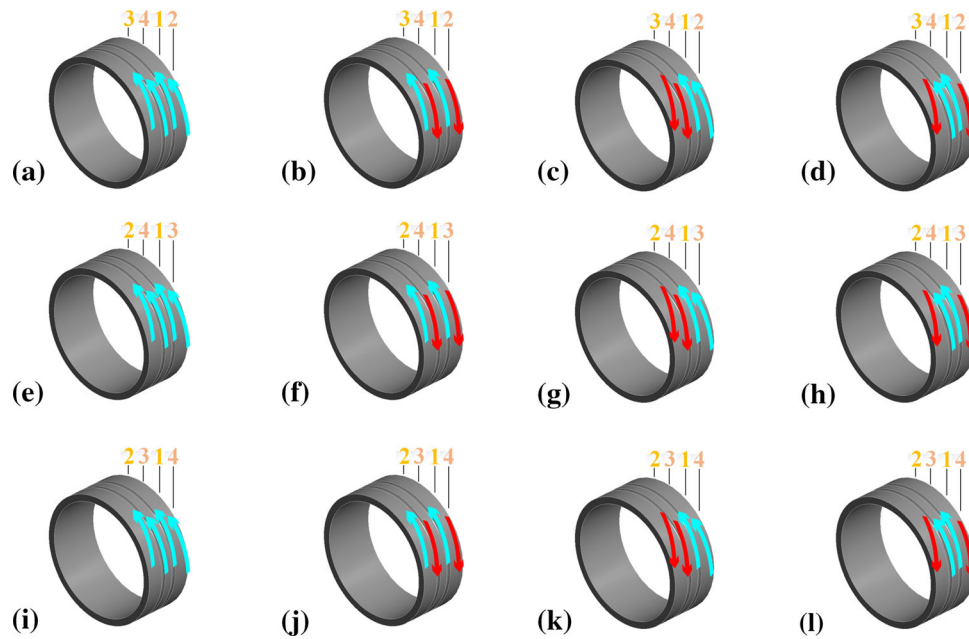


Fig. 8 Scanning strategies

carried out by synchronized powder feeding, and the cladding system is shown in Fig. 10.

According to the finite element model determined by size parameters, the grooves occupy less surface area of the annular thin-walled part. Therefore, the model is established and then meshed to reduce the calculation cost and improve the accuracy. The model mesh is divided into three regions: cladding layer zone (I), substrate proximal zone (II) and substrate distal zone (III). The substrate distal zone has the largest mesh size of the model, the grooves in substrate proximal zone is close to the cladding layer and the mesh sizes of the cladding layer zone is the smallest at last. The mesh sizes of each region are shown in Table 6.

There are 356,836 nodes and 73,380 elements in the single-layer and single-track finite element model after meshing. And there are 545,836 nodes and 106,860 elements in the multi-layer and multi-track finite element model ($t_i = 2$, $l_j = 2$), as shown in Fig. 11.

3.2 Results

3.2.1 Single-Layer and Single-Track. Figure 12(a) illustrates the three-dimensional profile of a single-layer and single-track laser cladding for the radial grooves with a rectangular spot. The laser heat source is uniformly rotating on one of the radial grooves over time. Figure 12(b) depicts the spot top view of the temperature field simulation results of the single-layer and single-track. As evident from Fig. 12(b), the front area of the molten pool experiences an increase in temperature with the approach of the laser heat source, and the isotherms in the area are more densely packed. Upon leaving the vicinity of the laser, the temperature in the area far away from the heat source plummets dramatically, resulting in the formation of a dense head and sparse tail droplet molten pool. Subsequently, the area undergoes rapid heat spreading and the molten pool promptly transforms into a cladding layer with the departure of the heat source.

Figure 12(c) shows the axial cross section of cladding layer, where CZ is the cladding zone, MZ is the melting zone, HAZ is

the heat affected zone and SZ is the substrate zone. It can be seen from the cross section that the temperature gradient is divided into eight regions. The temperature gradient decreases successively from the first region at the top of the cladding layer to the ninth region at the bottom of the substrate. The powder on the surface of the cladding is directly irradiated by the laser heat source, which leads to the maximum heat exposure. The first region of temperature gradient is part of the seventh region is uniformly distributed in CZ. The laser heat source instantly passes through the CZ to reach the interior of the substrate, resulting in the melting of the coating powder and the substrate surface. The melting zone forms MZ and the temperature gradient reveals that most of the seventh region is in MZ. The surface of the groove increases the powder contact area, which makes the substrate surface receive more diffusion heat. The heat causes changes in the microstructure of the substrate, which belongs to HAZ. HAZ with the eighth region is semi-elliptical in small area. The substrate temperature decreases gradually with the increase in the distance from the cladding layer. The bottom of the substrate is least affected by heat and the temperature gradient is also in the ninth region. Figure 12(d) illustrates the maximum temperature evolution of single-layer and single-track. After the laser scanning starts, the maximum temperature of the cladding layer rises rapidly and fluctuates periodically in a small temperature range until the scanning is completed. After the laser heat source is scanned for one circle (20 s), the maximum temperature of the cladding layer reaches 1498.7 °C and remains at about 1490 °C, which far exceeds the melting point of 316L stainless steel powder (1370 °C). The 316L stainless steel powder irradiated by laser heat source melts with the groove to form a molten pool. At the end of the scanning, the temperature drops rapidly and then cools for 100 s to normal temperature.

This paper utilizes sampling analysis to observe the temperature change of a single-layer and single-track cladding layer more easily and clearly at different times when the parameters are set. The temperature field of the laser cladding process is analyzed by selecting five nodes of m1-m5 at the

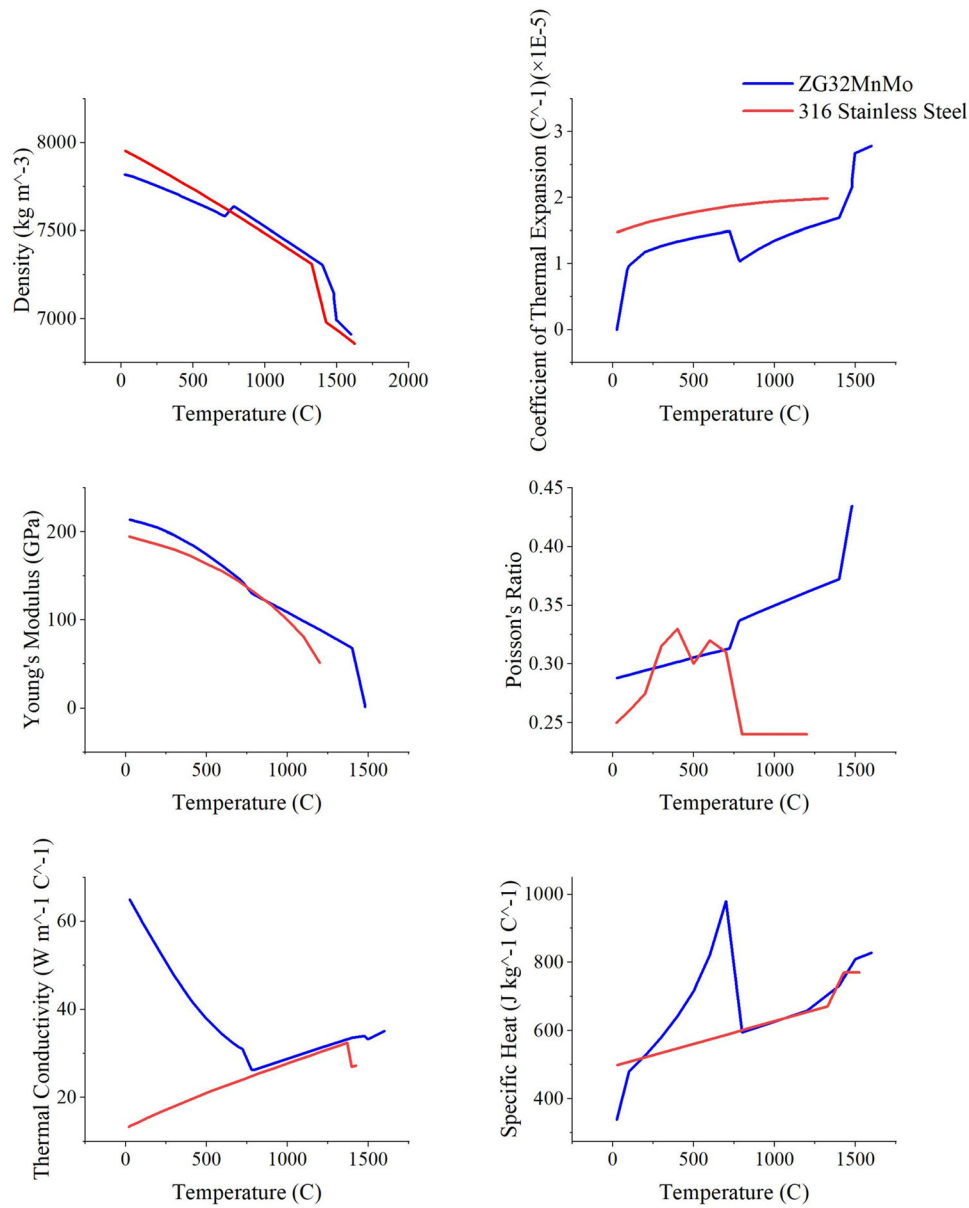


Fig. 9 Material characteristic parameters

Table 3 The chemical composition of 316L stainless steel powder

Elements	C	Si	Mn	S	P	Cr	Ni	Mo
Wt.%	≤ 0.03	≤ 1.00	≤ 2.00	≤ 0.03	≤ 0.045	16-18	10-14	2-3

Table 4 The powder parameters of 316L stainless steel powder

Powder parameters	Values
Mean diameter, μm	26
D10, μm	19.4
D50, μm	29.1
D90, μm	41.6

Table 5 Process parameters of laser cladding

Laser parameters	Values
Power, P , W	2300
Scanning speed, V_t , mm/s	26
Powder feed rate, V_f , g/min	40
Rectangular spot length, B , mm	12
Rectangular spot width, L , mm	2

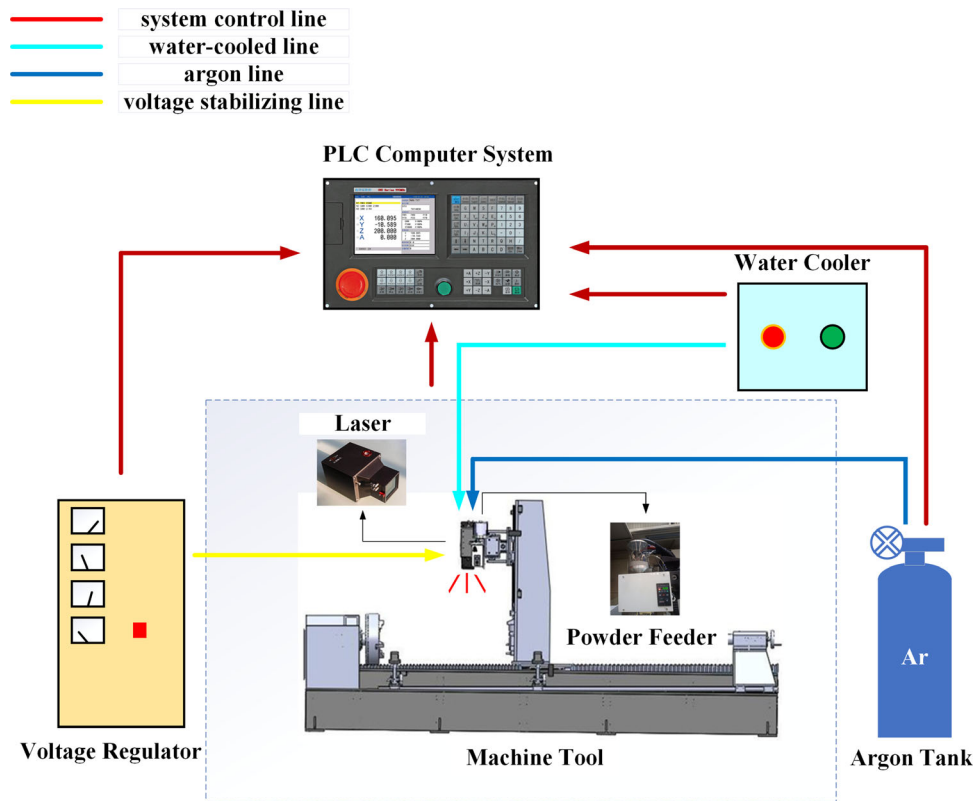


Fig. 10 Laser cladding systems

Table 6 Regions and mesh size

Regions, mm × mm × mm	length × width × height, mm × mm × mm	Mesh sizes
Cladding layer zone, I		1 × 1 × 1
Substrate proximal zone, II		1 × 0.9 × 2.3
Substrate distal zone, III		1.5 × 1 × 2.3

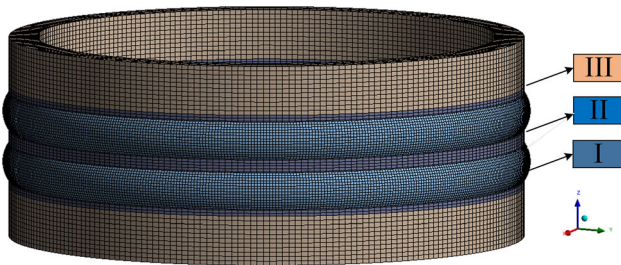


Fig. 11 Finite element mesh model of multi-layer and multi-track

cladding layer and four moments of the scanning period. Finally, the maximum temperature distribution of all the sampling points of the model is generated. Figure 13(a) shows the time variation of the temperature of the five nodes on the model surface. Figure 13(b) depicts the schematic diagram of model sampling points and Fig. 13(c) displays the three-dimensional profile of the cladding layer at four moments. Among them, the five nodes are uniformly distributed in the single cladding layer and the point m1 is not only the initial point but also the end point of the single-layer scanning. The

first three of the four moments correspond to the laser heat source starting scanning from the initial point m1, passing through point m2, and finally returning to point m1. The last moment represents the time after cooling for 100 s.

When the laser heat source scans ($t = 0$ s), the rectangular spot starts from the initial point m1. Because it takes time for the laser power to reach the rated power in an instant, the maximum temperature of the initial point m1 cannot reach 1000 °C. After the laser leaves the point m1, the temperature of the point m1 drops rapidly. The heat source passes through the point m2-m5. The points m2 ($t = 4$ s), m3 ($t = 8$ s), m4 ($t = 12$ s) and m5 ($t = 16$ s) rise to the maximum temperature in turn under the irradiation of the laser, but all drop rapidly after the laser heat source leaves. At the end of single-layer scanning ($t = 20$ s), the rectangular spot returns to the initial point m1. The residual temperature of point m1 rises suddenly under the influence of the heat source, so the maximum temperature of point m1 increases. From the 50 s and 100 s cooling time of the radial cross section can be seen, the maximum temperature at point m1 drops sharply with the disappearance of the laser heat source and there is no sign of rising again. After 100 s cooling time, the temperature of cladding layer gradually decreased to normal temperature. This phenomenon fully reflects the instantaneous thermal motion (such as laser cladding process) characteristics of temperature rising and falling fast.

Figure 14(a) describes the total residual stress distribution of single-layer and single-track laser cladding for the radial grooves of annular thin-walled parts. The stress of the groove surface is higher, but the residual stress of the whole substrate is much lower than that of the cladding area.

Figure 14(b) reveals total and three-dimensional residual stress evolution of single-layer and single-track laser cladding

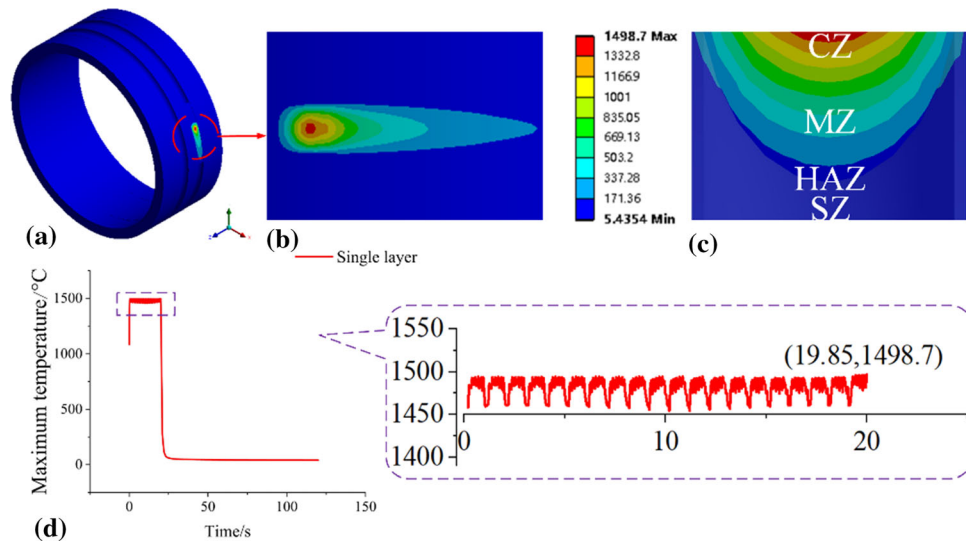


Fig. 12 Temperature evolution and distribution of single-layer and single-track laser cladding for radial grooves of annular thin-walled parts with rectangular spot: (a) three-dimensional profile, (b) spot top view, (c) temperature distribution of an axial cross section of cladding layer and (d) maximum temperature evolution

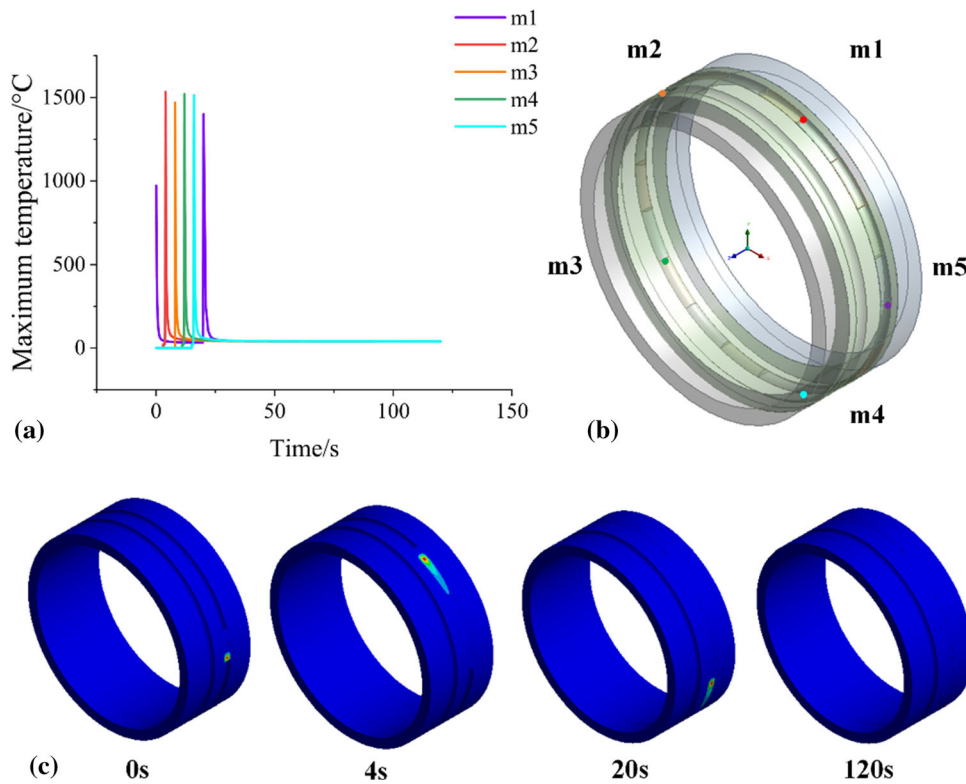


Fig. 13 Temperature evolution and distribution of model sampling points and moments in single-layer and single-track laser cladding for radial grooves of annular thin-walled parts with rectangular spot: (a) temperature evolution of model sampling points, (b) schematic diagram of model sampling points and (c) temperature distribution of four moments in the process of laser movement

for radial grooves of annular thin-walled parts. In general, the temperature of the heated area rises rapidly and begins to expand freely when the laser heat source is close to a certain area of the cladding layer, which expands outward along the cladding scanning direction (lateral) to form a tensile stress. The cladding layer is thermally expanded to squeeze the unformed part and the groove on the substrate, so that the stress along the substrate thickness direction (radial) and perpendic-

ular to the cladding scanning direction (axial) is compressive stress (Ref 32). It can be seen from Fig. 14(b) that when the Z-axis is taken as the axial direction and the radial groove is taken as the cladding object, the lateral and radial directions of the annular thin-walled part cannot completely correspond to the X-axis and Y-axis. The scanning direction of the laser cladding rotates in the XOY plane with the uniform rotation of the laser heat source, which leads to the continuous change of the lateral

and radial direction in the XOY plane. Therefore, the stress change in the X-axis and Y-axis is much larger than that in the Z-axis. The tensile stress and compressive stress of X-axis and Y-axis are also changing when the cladding layer rotates laterally and radially on the XOY plane, so the total stress shows a stable periodic fluctuation trend in a certain range. At the end of the scanning, the laser heat source returns to the initial point, which causes the initial area of incomplete thermal diffusion to heat again. The phenomenon of heat accumulation occurs rapidly the stress is concentrated again due to thermal expansion. And then the total and three-dimensional stress increases to the maximum. However, the temperature decreases continuously after the laser heat source disappears. The lateral stress begins to develop into compressive stress, but the radial and axial stress changes into tensile stress. The residual stress decreases rapidly and tends to be stable while the molten pool is gradually solidifying to form a cladding layer. When the laser heat source returns to the initial point of the last layer, the maximum stress reaches 422.89 MPa. The Y-stress is the largest, followed by the X-stress and the Z-stress is the smallest among the three-dimensional stress.

In this paper, the path perpendicular to the cladding scanning direction (axial) is selected as Path1 and the path in the direction of substrate thickness (radial) is selected as Path2 for the detailed change of residual stress in all directions. The stress distribution of the substrate and cladding layer is observed after cooling for 100 s, as shown in Fig. 15(a). Figure 15(b-c) displays the stress evolution of Path 1 and Path 2.

As can be seen from Fig. 15(b), the stress on the substrate increases with the close of the distance near the cladding layer.

The stress reaches the maximum at the top of the groove and then the stress decreases. There is a peak stress in the total stress curve due to the constraint of grid zone. But after that, the stress continues to decrease until it reaches the minimum when it is away from the cladding layer 11 mm and then the stress increases gradually. The partial stress in the triaxial direction is all in the base region and the variation rule of the triaxial stress curve is similar: At this time, the substrate is heated and expanded by the nearby cladding layer, which is tensile stress. The tensile stress decreases with the heat source away from the groove cladding layer. The substrate bears the opposite tensile stress due to the constraint and cold shrinkage principle on both sides with the increase in the distance, so the total stress rises again. Finally, the constraint decreases with the increase in the distance away from the cladding layer, so the stress recovery trend is gradually reducing.

As can be seen from Fig. 15(c), the residual stress on the surface of cladding layer directly irradiated by laser heat source is the largest. But the stress decreases with the deepening of the groove depth. At the bottom of the groove, the stress reduction trend of substrate obviously slows down because of the different characteristics of cladding and substrate. The lower surface of the substrate expands into the interior due to thermal diffusion, so the stress increases suddenly with the deepening of the substrate depth. The partial stress in the triaxial direction of X, Y and Z is basically in the cladding layer and the substrate region. The Y-stress and Z-stress manifest tensile stress due to thermal expansion in the cladding layer. The difference is that the Y-stress decreases because it is gradually far away from the laser heat source, but the Z-stress increases. While the X-stress is constrained by the substrate groove, it presents a gradually

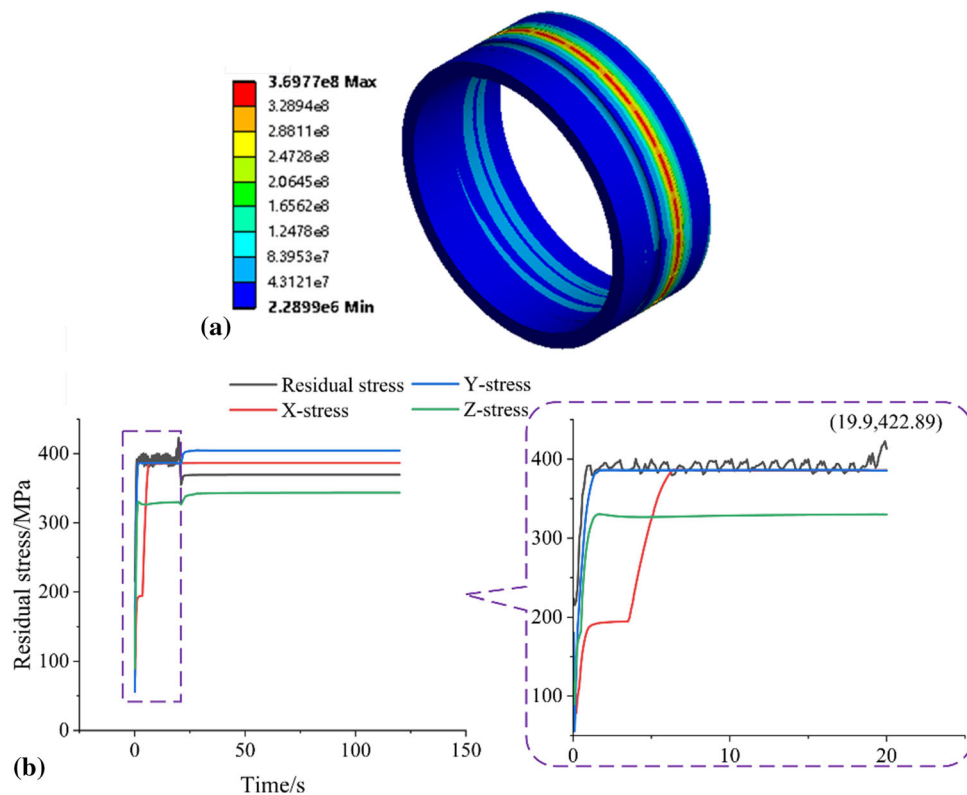


Fig. 14 Residual stress evolution and distribution of single-layer and single-track laser cladding for radial grooves of annular thin-walled parts with rectangular spot: (a) total residual stress distribution and (b) total and three-dimensional residual stress evolution

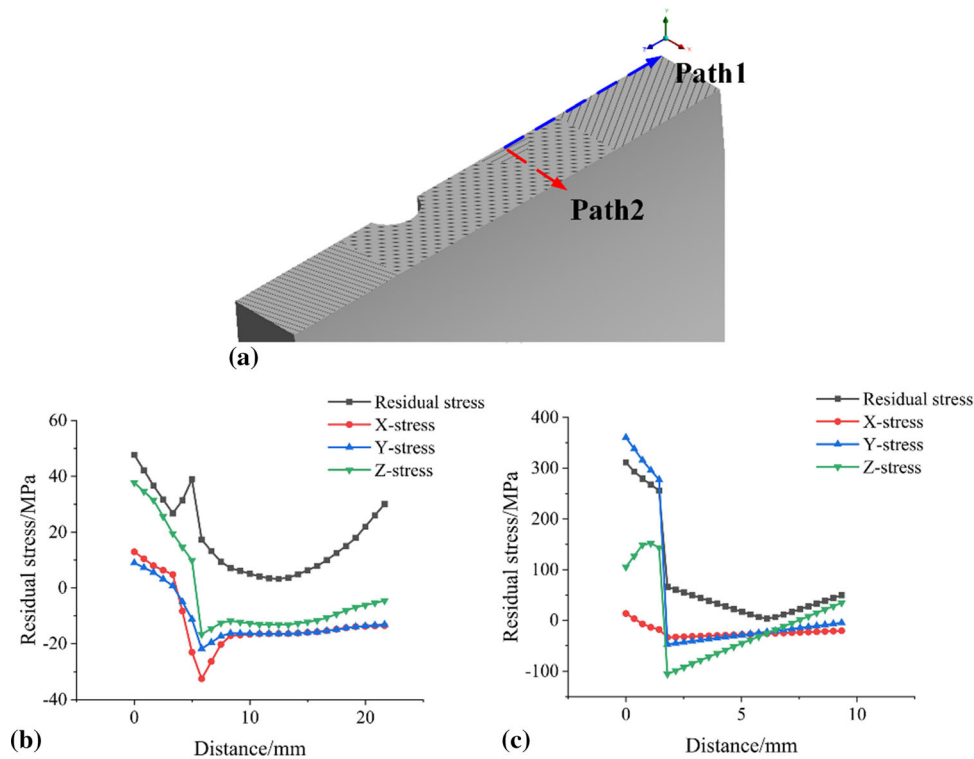


Fig. 15 Residual stress evolution of single-layer and single-track cladding layer of sampling path on the cross section: (a) schematic diagram of sampling path, (b) residual stress evolution of path 1 and (c) residual stress evolution of path 2

increasing compressive stress. In the substrate region, the triaxial stress is compressive stress at first and then it is transformed into tensile stress because of the internal thermal expansion.

Figure 16 shows the total and three-dimensional deformation evolution of the substrate. The total deformation is kept at about $10\ \mu\text{m}$ in the process of cladding. X-deformation and Y-deformation basically follows the law of circular distribution. The sum of the vectors is the deformation of the base on the XOY plane. The law of displacement change in Z-axis direction is like the total deformation, but Z- deformation is smaller. At the end of the scanning, the total and three-dimensional substrate deformation evolution stop quickly due to the loss of the laser heat source. The total substrate deformation is $105.9\ \mu\text{m}$ after cooling for 100 s.

Experiments are carried out with the parameters set during simulation. The experimentally obtained fused cladding layer is cut along the vertical scanning direction and processed to obtain a cross section. The cross section is compared with the cross section of the numerically simulated fused cladding layer as shown in Fig. 17. As can be seen in Fig. 17, it is found that the cross sections of the fused cladding layer are well formed morphologically.

The maximum values of simulation (referred to as Sim) and experimental (referred to as Exp) deformations in Table 7 reach $105.9\ \mu\text{m}$ and $99\ \mu\text{m}$, respectively. The error between simulation and experiment is within 10%. It proves the accuracy of the thermal coupling simulation model in this study. The deformation of X-axis under the experiment is $61\ \mu\text{m}$, Y-deformation is $54\ \mu\text{m}$, and Z-deformation is $56\ \mu\text{m}$. The overall relative errors (referred to as RE) between the simulation and experimental results are all within 10% in absolute value, with a mean relative error (referred to as MRE) of 4.88%. It further proves

the accuracy of the results of the optimal parameter combination.

To sum up, the reliability of the model is verified by the numerical simulation of single-layer and single-track laser cladding for the radial grooves of annular thin-walled parts. The set laser cladding process parameters can be selected as the optimal parameters for the numerical simulation test of multi-layer and multi-track.

3.2.2 Comparison of Single-Layer and Multi-Track under Different Scanning Strategies. To observe and analyze the influence of cold and heat overlapping on the deformation of the radial grooves, multi-layer and multi-track is divided into single-layer and multi-track, multi-layer and single-track. When only single-layer and multi-track is considered ($t_i = 2, l_j = 1$), there are only two scanning strategies: HT and CT. Therefore, it is necessary to compare the effects of the two scanning strategies on the deformation.

Figure 18 depicts the maximum temperature evolution comparison of single-layer and multi-track laser cladding scanning strategies. As can be seen from Fig. 17, the temperature curve is basically consistent with the thermal cycle curve of single-layer and single-track in the first laser scanning process (20 s). The maximum temperature of the cladding layer reaches $1499\ ^\circ\text{C}$ and fluctuates periodically at about $1490\ ^\circ\text{C}$. The overall temperature drops rapidly after the end of the first laser scanning. But the laser heat source quickly begins to carry out the second laser scanning on the second groove and the temperature rises again.

There are differences between the two scanning paths in the second laser scanning. The laser scan along the opposite path, respectively. The two-temperature evolution almost coincides with each other but there is no obvious difference. In addition, although the first laser scanning preheats the annular thin-

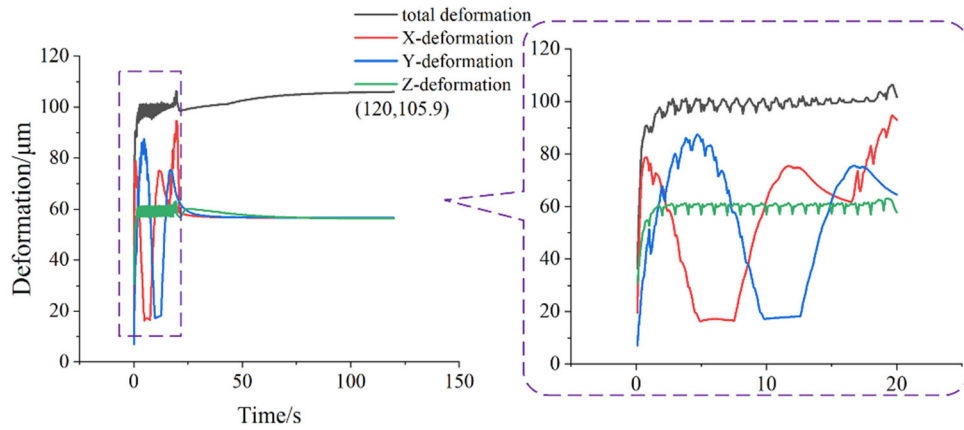


Fig. 16 Total and three-dimensional deformation evolution of single-layer and single-track laser cladding for the substrate

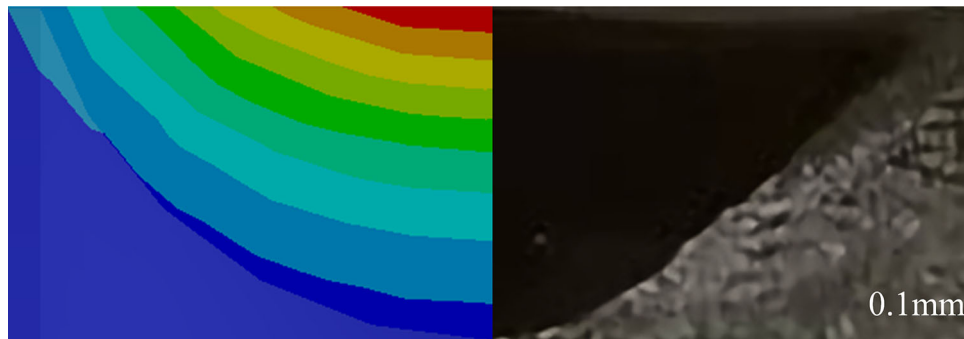


Fig. 17 Comparison between simulation and experiment fused cladding layer cross section for single-layer and single-track

Table 7 Comparison of simulation and experiment deformations of single-layer and single-track

	Total deformation	X-deformation	Y-deformation	Z-deformation
Sim, μm	105.9	56.4	56.5	56.2
Exp, μm	99	61	54	56
RE	- 6.97%	7.54%	- 4.63%	- 0.36%
MRE	4.88%			

walled part, the overall temperature change of the second cladding layer is almost the same as that of the first cladding layer. The maximum temperature of the cladding layer reaches 1505 °C, which also keeps fluctuating periodically at around 1490 °C. The groove spacing affects the thermal diffusion of the first cladding layer to the second groove. The second groove is less heated and only produces little heat accumulation. The temperature change is almost not affected by the first laser scanning. The substrate is cooled to normal temperature for 100 s at the end of the second laser scanning. The maximum temperature evolutions under the two scanning strategies are roughly the same, but the temperature trend of CT is obviously lower than that of HT from the end time.

Figure 19 illustrates the residual stress evolution comparison of single-layer and multi-track scanning strategies. As can be seen from Fig. 18, the temperature in the heated area rises rapidly and begins to expand freely to form stress after the beginning of the first laser scanning. The stress evolution trend

is roughly consistent with that of the single-layer and single-track.

In the second laser scanning, the stress of the two scanning paths increases rapidly. It continues to fluctuate periodically in a certain range when it rises to 450 MPa. It can be seen from Fig. 18 that the stress field more clearly reflects the heat accumulation phenomenon of the second cladding layer absorbing the heat of the first cladding layer than the evolution of the temperature field. The heat accumulation makes the cladding layer form more stress during the second laser scanning, so the overall trend is higher than that of the first cladding layer. At the end of the second laser scanning circle, the laser heat source disappears. The residual stress decreases rapidly and tends to be stable. It is known that the residual stress evolutions under the two scanning strategies are basically the same from the end time, but the residual stress trend of CT is obviously lower than that of HT.

Figure 20 proves the total deformation evolution comparison of single-layer and multi-track scanning strategies.

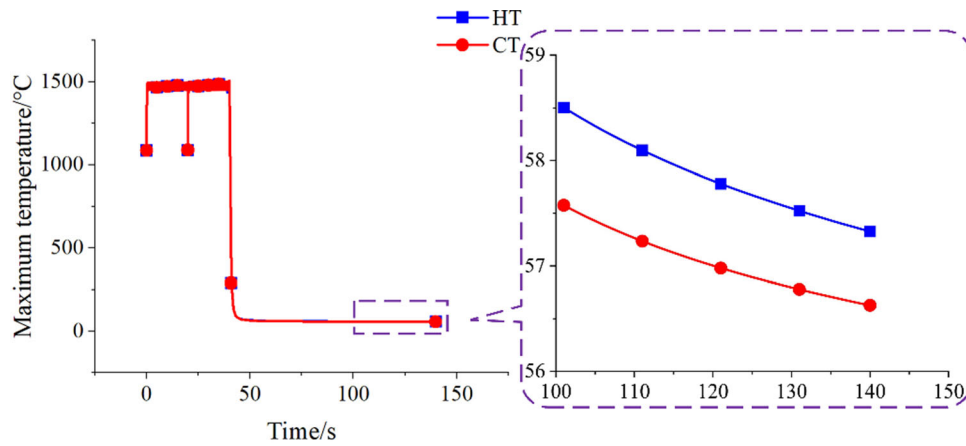


Fig. 18 Comparison of temperature evolution of single-layer and multi-track

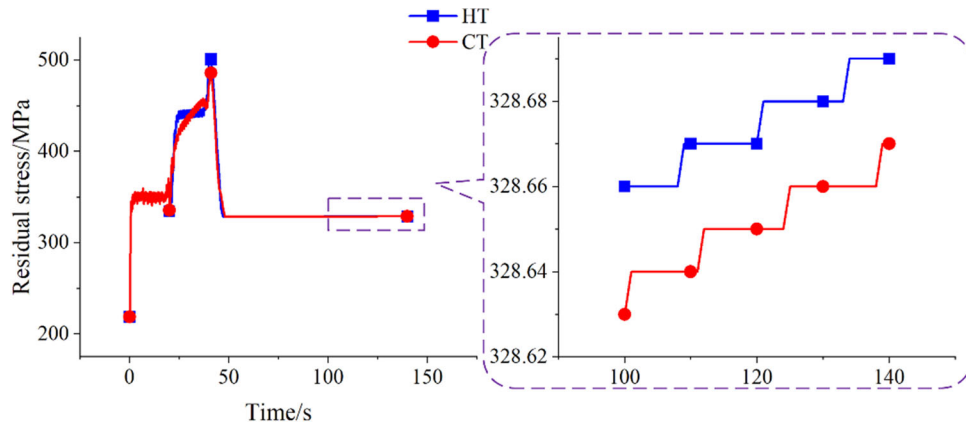


Fig. 19 Comparison of residual stress evolution of single-layer and multi-track laser cladding

Because the thermal deformation of the substrate is mainly caused by the uneven extrusion of the thermal stress of the cladding layer, the deformation is deeply affected by the residual stress. The evolution trend is roughly the same as that of stress. The residual stress tends to be stable rapidly after the laser heat source disappears and the substrate gradually shrinks. From the end time, the deformation of CT is 121.8 μm , which is slightly lower than that of HT 122.7 μm . It is known that cold overlapping and hot overlapping have little influence on the radial groove deformation for the single-layer and multi-track. The reverse scanning path of CT relatively reduces the phenomenon of heat accumulation in the same direction, so that the stress distribution of the substrate is more uniform than that of HT. Therefore, the substrate deformation is relatively small. Finally, the scanning strategy of CT is better than that of HT.

3.2.3 Comparison of Multi-Layer and Single-Track under Different Scanning Strategies. In the case of only considering multi-layer and single-track ($t_i = 1, l_j = 2$), it is necessary to compare the effects of multi-layer hot overlapping and multi-layer cold overlapping on the deformation are consistent.

Figure 21 demonstrates the maximum temperature evolution comparison of multi-layer and single-track scanning strategies. As can be seen from Fig. 21, the maximum temperature evolution trend caused by the first laser scanning is roughly consistent with that of single-layer and single-track.

In the second laser scanning, the two scanning paths diverge and the laser heat source is still scanning along the opposite path. Different from the case of single-layer and multi-track, the periodic fluctuation trend of the second cladding layer temperature evolution is much larger than that of the first one. In the process of the second laser scanning, because the second laser scanning continues cladding immediately on the first cladding layer, so the thermal diffusion phenomenon does not fully occur in the cladding layer. The first cladding layer plays a preheating role for the second cladding layer. Hence, the residual temperature of the first cladding layer and the substrate is much higher than the normal temperature of the substrate surface during the first cladding, resulting in a small amount of heat accumulation in the second laser cladding. The heat accumulation is the reason why the periodic fluctuation trend of the second cladding layer temperature evolution is much larger than that of the first layer. The temperature rises rapidly to 2300 $^{\circ}\text{C}$ and the maximum temperature can reach 2456.2 $^{\circ}\text{C}$. On the other hand, the reverse scanning path of CL causes the laser to re-pass immediately through the cladding area that has just left, so the phenomenon of heat accumulation is more than that of HL. Therefore, the periodic fluctuation trend of the second cladding layer temperature evolution of CL is also much higher than that of HL. The substrate is cooled to normal temperature for 100 s at the end of the scanning. From the end time, the temperature trend of CL is higher than that of HL.

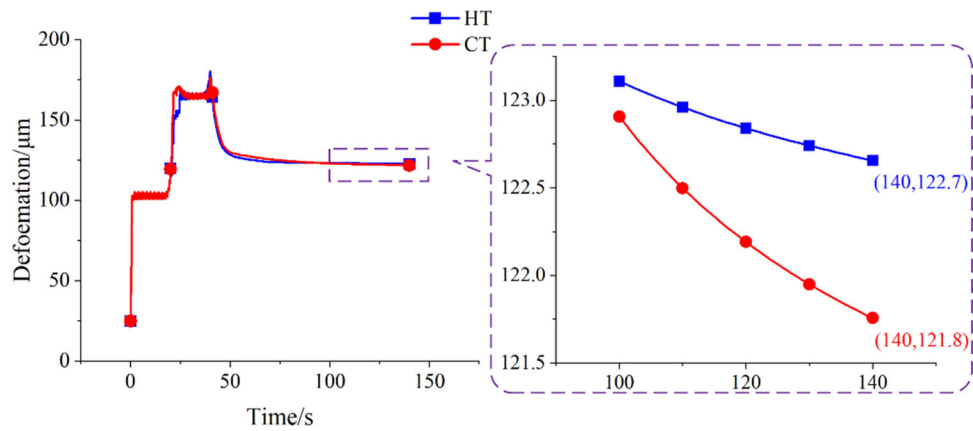


Fig. 20 Comparison of deformation evolution of single-layer and multi-track laser cladding

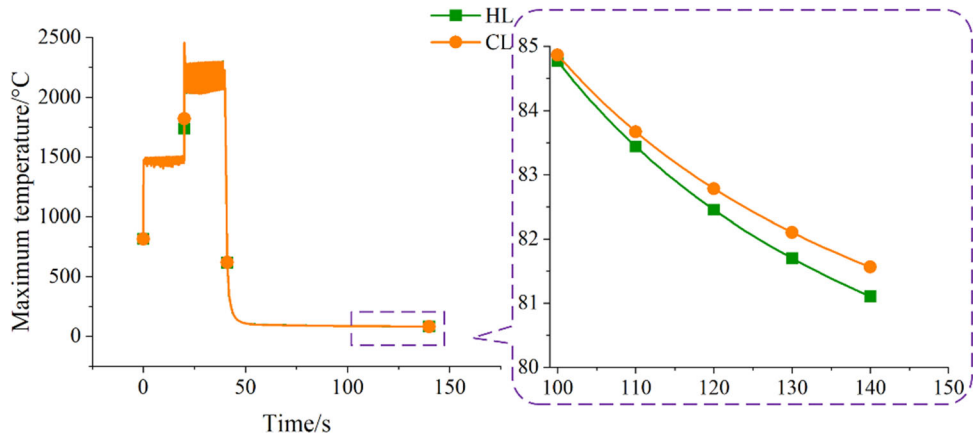


Fig. 21 Comparison of temperature evolution of multi-layer and single-track laser cladding

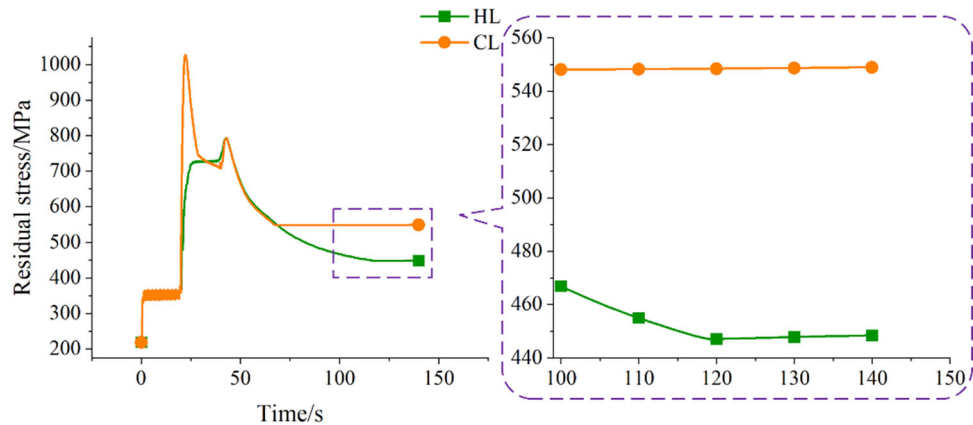


Fig. 22 Comparison of residual stress evolution of multi-layer and single-track laser cladding

Figure 22 shows the residual stress evolution comparison of multi-layer and single-track scanning strategies. As can be seen from Fig. 22, the stress evolution trend is still roughly consistent with that of the single-layer and single-track.

In the second laser scanning, the stress evolutions of the two scanning paths are obviously different. The total stress rises with the increase in cladding times in the case of HL, so the stress of the second laser cladding is much higher than that of

the first one. The periodic fluctuation of stress in the upper layer is more stable than that in the next layer for the preheating role of the first cladding layer. Finally, it reaches the maximum stress 727 MPa due to the heat accumulation in the initial region when the laser heat source returns to the initial region of the last layer. The stress of CL passes immediately through the newly left cladding area when the second laser scanning is reversed. The heat accumulation leads to the thermal expansion

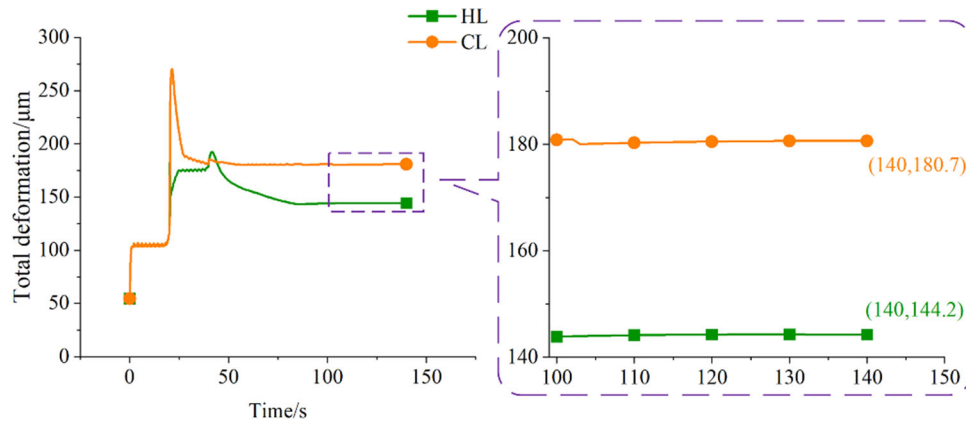


Fig. 23 Comparison of deformation evolution of multi-layer and single-track laser cladding

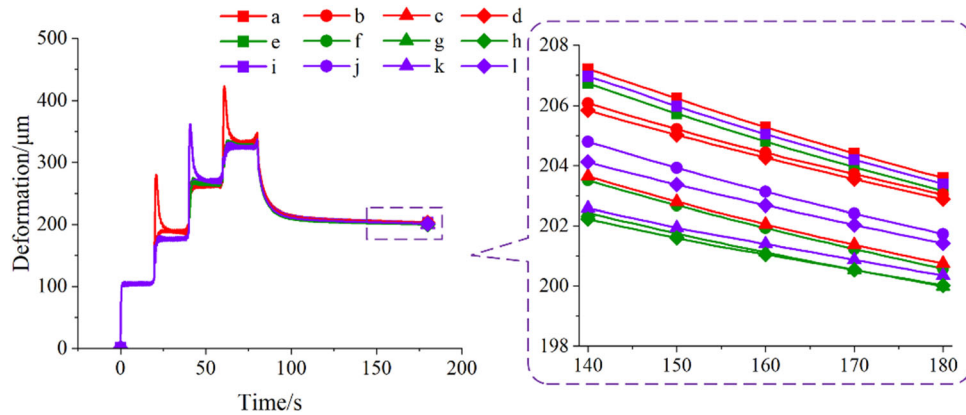


Fig. 24 Comparison of total deformation evolution of multi-layer and multi-track laser cladding under different scanning strategies

of the incompletely cooled cladding layer again. The total stress gets the maximum stress 1026 MPa instantly, which is much larger than the maximum stress of HL. The total stress decreases in the second laser scanning time with the departure of the laser heat source. But it rises still briefly due to the heat accumulation when the laser heat source returns to the initial region of the last layer. At the end of scanning and cooling for 100 s, the residual stress decreases rapidly and tends to be stable with the disappearance of laser heat source. From the end time, the residual stress of CL is obviously higher than that of HL.

Figure 23 displays the total deformation evolution comparison of multi-layer and single-track scanning strategies. The evolution trend is generally consistent with that of stress. From the end time, the deformation of HL is 144.2 μm , which is lower than 180.7 μm of CL. Cold overlapping and hot overlapping have a great influence on the radial groove deformation for the multi-layer and single-track. The reverse scanning path of CL relatively increases the heat accumulation, so that the uneven distribution of stress in substrate is much greater than that of HL. Hence, the substrate deformation is relatively large. Finally, the scanning strategy of HL is better than that of CL.

3.2.4 Comparison of Multi-Layer and Multi-Track under Different Scanning Strategies. Figure 24 describes the deformation and displacement evolution of multi-layer and

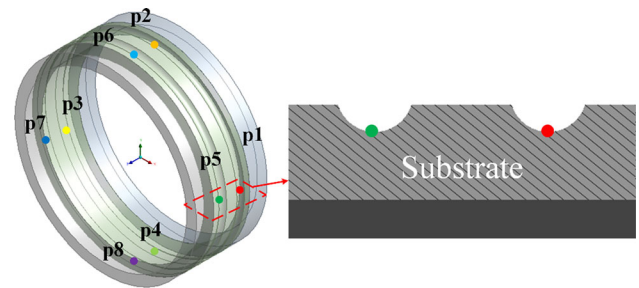


Fig. 25 Schematic diagram of model sampling points of multi-layer and multi-track laser cladding for radial grooves of annular thin-walled parts with rectangular spot

multi-track for the radial grooves under 12 scanning strategies. As can be seen from Fig. 24, the substrate deformation reaches the minimum depending on the scanning strategy (g).

As shown in Fig. 25, eight nodes, such as point p1-p8, are selected at the bottom of the radial grooves to observe the total deformation evolution of the substrate more conveniently and clearly. The evolution diagrams of maximum temperature, residual stress and total deformation of multi-layer and multi-track at different positions are generated.

Figure 26 exhibits the temperature evolution of the sampling point position varying with time under different scanning

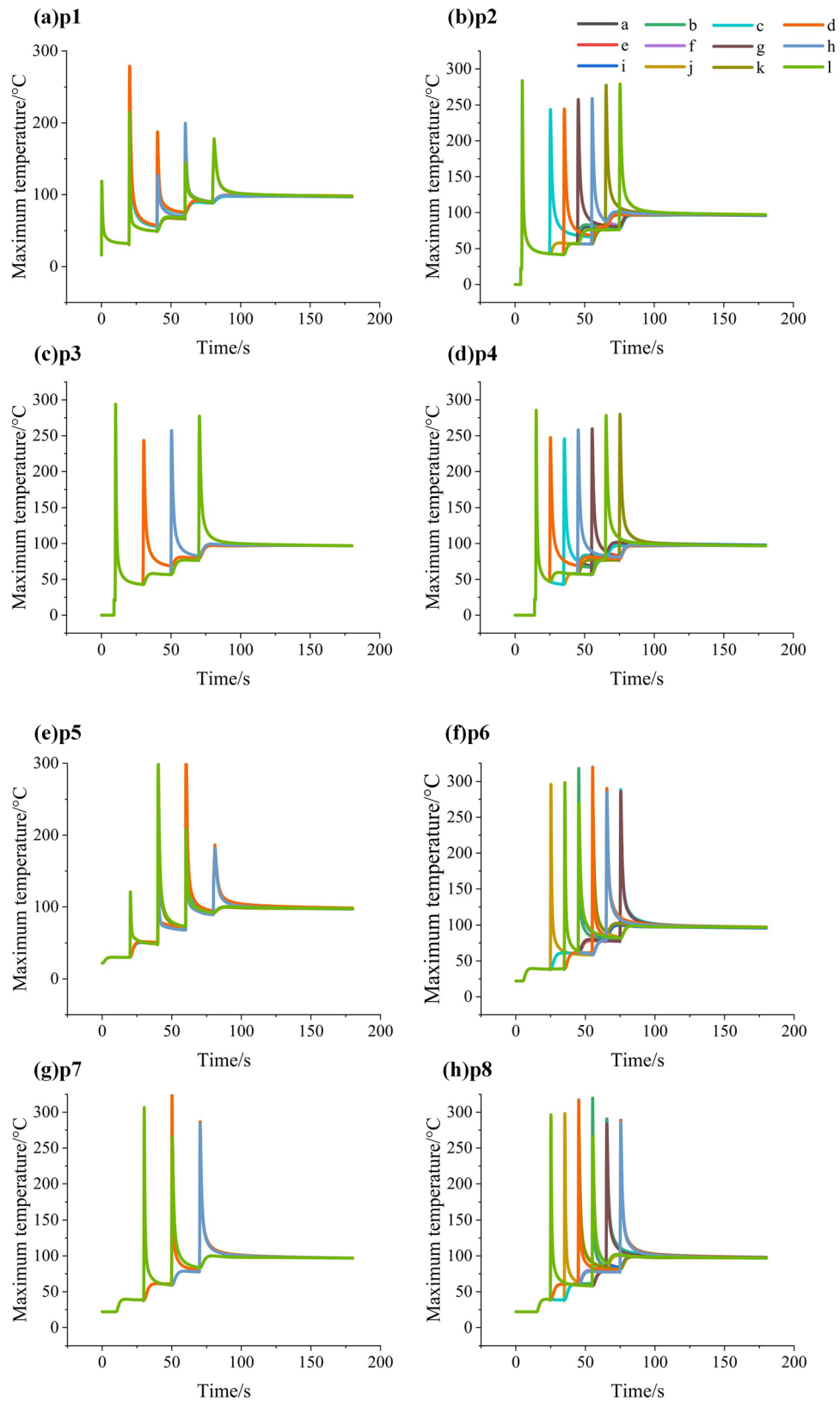


Fig. 26 Temperature evolution of sampling point (p1-p8) of multi-layer and multi-track laser cladding under different scanning strategies

strategies. As can be seen from Fig. 26 (p1-p8), the temperature changes of each sampling point are similar. The temperature of the point rises rapidly and reaches the maximum when the laser heat source is close to the sampling point. But then the

temperature decreases rapidly with the departure of the heat source. The temperature of the parallel sampling point on the adjacent grooves increase to a certain extent when the laser heat source sweeps through a sampling point. Because the groove

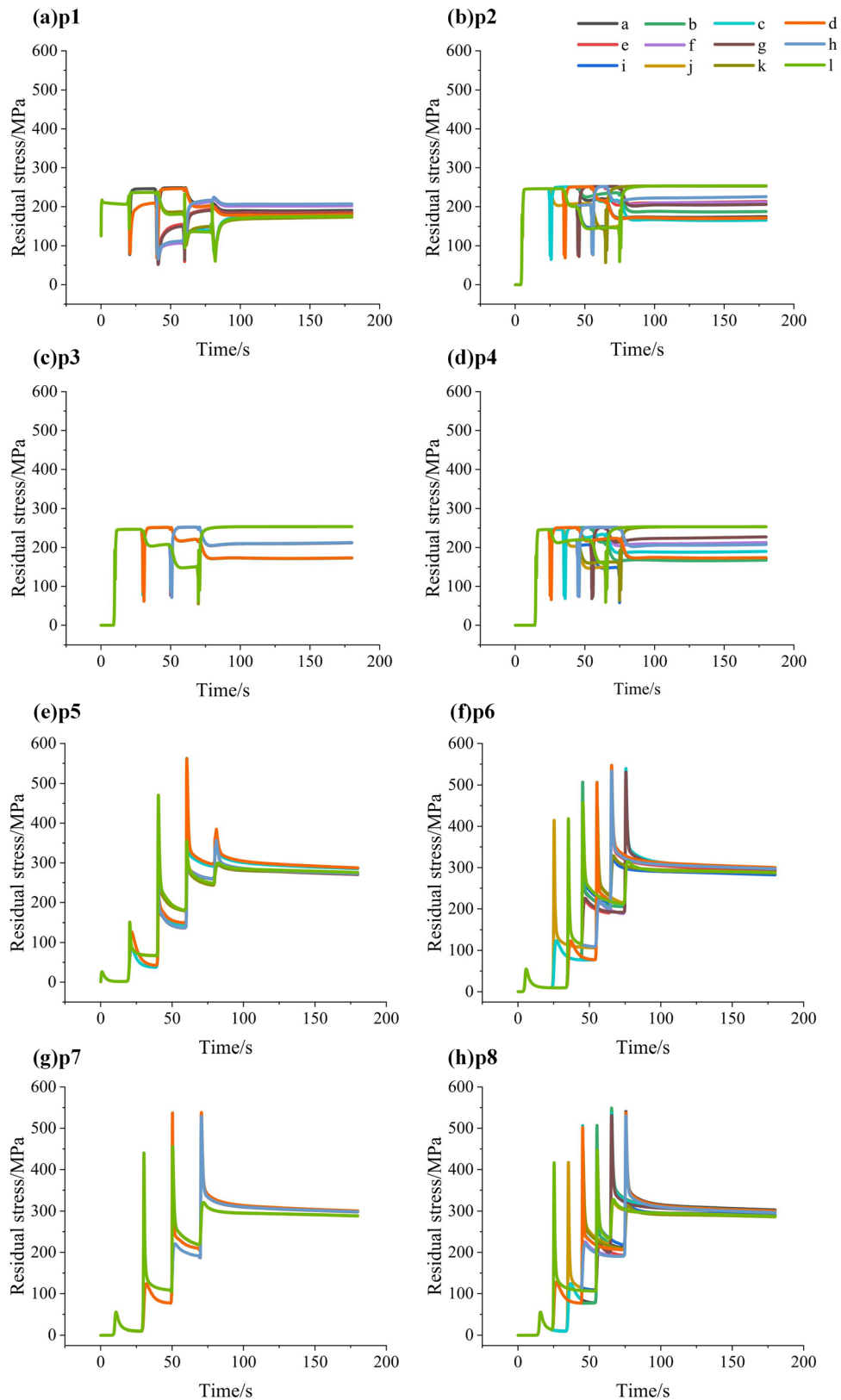


Fig. 27 Residual stress evolution of sampling point (p1-p8) of multi-layer and multi-track laser cladding under different scanning strategies

spacing slows down the heat diffusion between the grooves, there is only less heat diffusion to the parallel sampling points. The heat diffuses from the cladding layer inside to the groove surface when the laser heat source sweeps near the upper part of

a sampling point, so that a rising temperature peak appears again in Fig. 26.

Figure 27 shows the residual stress evolution of the sampling point position changing with time under different

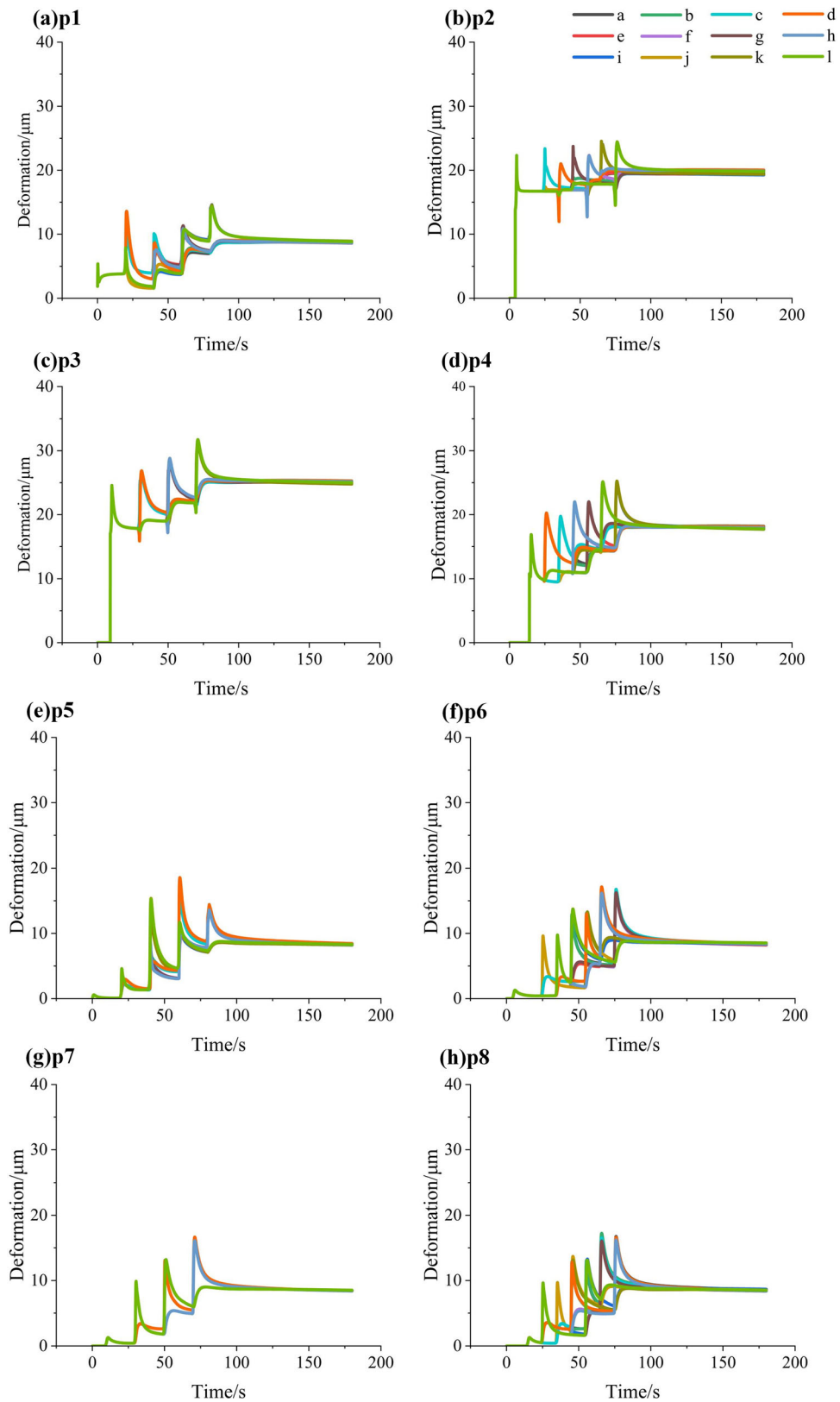


Fig. 28 Deformation evolution of sampling point (p1-p8) of multi-layer and multi-track laser cladding under different scanning strategies

scanning strategies. It can be seen from Fig. 27 (p1-p8) that the variation of residual stress at each point in the case of multi-layer and multi-track is consistent with that of single-layer and multi-track and multi-layer and single-track. There is an

obvious peak stress at the p5-p8 point relative to the p1-p4 points. When the first laser heat source scans through the sampling point (p1-p4) set on the first groove, a small amount of heat is diffused to the parallel sampling points between the

adjacent grooves (p5-p8 points) to preheat these points. Hence, the p5-p8 point still has peak stress due to thermal expansion, even if the laser heat source does not pass through them. The heat accumulation directly leads to the sudden increase in stress and reaches the maximum peak when the laser heat source is truly close to the p5-p8 points. This is the reason why the stress variation trend of the p1-p4 points is much more stable than that of the p5-p8 points.

Figure 28 depicts the total deformation evolution of the sampling point position changing with time under different scanning strategies. As can be seen from Fig. 28 (p1-p8), the variation of deformation at each sampling point is like that of stress. The point is heated and expanded when the laser heat source is close to the sampling point. And then it begins to cool with the departure of the laser heat source. A small amount of heat diffuses to the adjacent groove when the laser heat source

turns to another groove for scanning, resulting in thermal deformation. The thermal accumulation phenomenon makes Fig. 28 reappear a rising peak of deformation when the laser heat source sweeps near the upper part of a sampling point.

Table 8 shows the sampling point (p1-p8) and total deformation results of multi-layer and multi-track under different scanning strategies. It can be seen from Table 8 that the minimum deformation of point p1 and f is scanning strategy (e), the minimum deformation of point p2, p3 and p5 is scanning strategy (i), the minimum deformation of point p4 is scanning strategy (k) and the minimum deformation of point p7, p8 and total is scanning strategy (g).

By comparing the results of single-layer and multi-track and multi-layer and single-track scanning strategies, it is known that increasing the number of cladding(l_i) causes more heat accumulation than increasing the number of groove(t_i), so the

Table 8 Sampling points (p1-p8) and total minimum deformation of multi-layer and multi-track laser cladding under different scanning strategies

Results, μm	p1	p2	p3	p4	p5	p6	p7	p8	Total
a	87.30	194.30	250.60	181.67	82.34	82.37	84.03	85.77	203.59
b	89.00	199.80	252.70	181.05	84.33	84.54	84.06	84.48	203.04
c	87.00	195.40	250.60	179.79	82.33	84.03	84.03	84.08	200.75
d	88.80	200.00	252.80	180.90	84.37	84.53	84.06	84.50	202.88
e	86.40	193.10	249.30	180.20	82.64	82.18	83.90	85.50	203.15
f	86.60	199.30	251.60	179.00	82.70	84.05	83.90	83.74	200.57
g	86.60	194.30	249.29	178.31	82.61	83.85	83.89	83.73	199.99
h	86.80	198.70	251.58	179.21	82.66	83.79	83.91	83.93	200.02
i	88.50	192.70	247.82	178.62	82.07	83.38	85.00	86.65	203.39
j	88.50	198.40	249.96	177.71	83.08	85.31	85.03	85.20	201.73
k	88.50	193.70	247.83	177.05	82.14	84.79	85.01	85.01	200.35
l	88.50	198.10	249.97	177.62	83.09	85.33	85.03	84.99	201.42

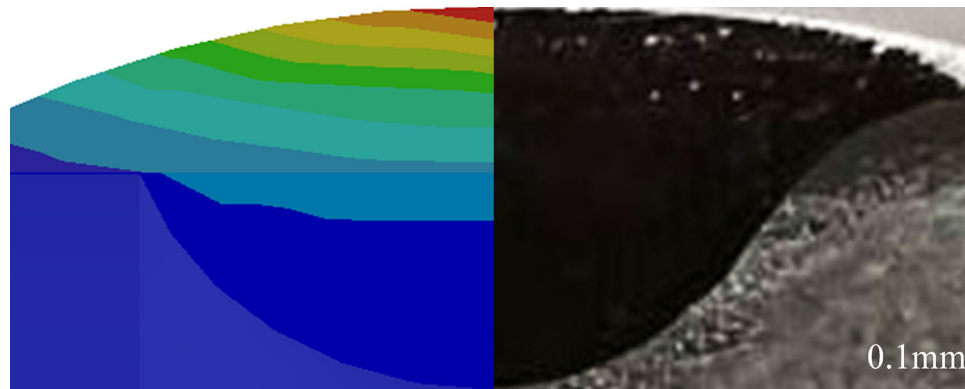


Fig. 29 Comparison between simulation and experiment fused cladding layer cross section for multi-layer and multi-track

Table 9 Comparison of simulation and experiment deformations of multi-layer and multi-track

	p1	p2	p3	p4	p5	p6	p7	p8	Total
Sim, μm	86.60	194.30	249.29	178.31	82.61	83.85	83.89	83.73	199.99
Exp, μm	83	202	228	191	80	87	90	77	210
RE	- 4.34%	3.81%	- 9.34%	6.64%	- 3.34%	3.62%	6.79%	- 8.95%	4.77%
MRE	5.73%								

influence of the tracks on deformation is not as obvious as that of the layers. Therefore, the results of the minimum deformation of the sampling points are all under the scanning strategies (e, i, g, k). They all adopt the scanning sequence of the layers first, then the tracks ($l_1t_1 \rightarrow l_1t_2 \rightarrow l_2t_1 \rightarrow l_2t_2$ or $l_1t_1 \rightarrow l_1t_2 \rightarrow l_2t_2 \rightarrow l_2t_1$) for laser cladding. These scanning strategies increase the cooling time of each cladding layer by magnifying the scanning interval of each cladding layer. Hence, the process of longer thermal diffusion time of the groove surface, more uniform heating and lower heat accumulation is caused, which reduces the deformation.

At the same time, the scanning strategy of HT-HL or CT-HL is adopted in the scanning strategy. Because cold overlapping and hot overlapping have little influence on the radial groove deformation of annular thin-walled parts for the single-layer and multi-track, both HT and CT may obtain the minimum deformation. Cold overlapping and hot overlapping have a great difference on the radial groove deformation for the multi-layer and single-track, so the scanning strategy with HL is still better than CL. The influence trend of cold overlapping and hot overlapping on the radial groove deformation for multi-layer and multi-track is consistent with the combination result of single-layer multi-track and multi-layer single-track. As a result, the scanning strategy with minimum heat accumulation can obtain the result of minimum deformation. The scanning strategy (g) is the optimal in two layers and two tracks, in which the cold overlapping between tracks first, and then the hot overlapping between layers. The scanning path is l_1t_1 (PD) \rightarrow l_1t_2 (ND) \rightarrow l_2t_1 (PD) \rightarrow l_2t_2 (ND) and the minimum deformation is 200 μm . The 12 scanning strategies do not change with the change increase or decrease in the cladding layer number (l_j) and groove number (t_i). Therefore, the scanning strategy (g) is still the best in multi-layer and multi-track.

Comparison of the fused cladding cross section between the multi-layer and multi-track simulation and experiment under scanning strategy (g), Fig 29 and Table 7 show that the delamination of each region corresponds accurately. It indicates that the cladding layer are well formed morphologically.

Fig 29 shows the comparison between the simulation and experimental results of the deformation amount at different sampling points (p1-p8) under the scanning strategy (g). The simulation results are consistent with the trend of the experimental results. Due to some measurement error in the actual measured experimental results, there is a certain deviation of the deformation between the various points. However, the overall deformation trend is consistent, and the fluctuation range is small.

As can be seen from Table 9, the overall relative errors between the simulation and experimental results are small, with a mean relative error of 5.73%. It indicates that the simulation and experimental results are more consistent and verifies the correctness of the scanning strategy (g).

4. Conclusion

A variety of circular cross-scanning strategy models are established. The influences of hot overlapping and cold overlapping for the temperature, stress, and deformation of radial grooves under different scanning strategies are obtained based on the thermal-mechanical coupling simulation.

- (1) The cladding zone shape of single-layer and single-track is water droplets and the maximum temperature is 1498.7 °C. The maximum value of residual stress is at the junction of cladding layer and the groove. The final simulated deformation is 105.9 μm . The experimental results are basically consistent with the simulation results, and the mean relative error is less than 10%.
- (2) Cold overlapping and hot overlapping have little influence on the radial grooves deformation of annular thin-walled parts for the single-layer and multi-track. The scanning strategy of cold overlapping between tracks (CT) is better than that of hot overlapping between tracks (HT). But cold overlapping and hot overlapping have a great influence on the deformation for the multi-layer and single-track. The scanning strategy of hot overlapping between layers (HL) is better than that of cold overlapping between layers (CL).
- (3) The scanning strategy (g) with the minimum heat accumulation has the result of minimum deformation under the twelve scanning strategies. The optimal scanning path is l_1t_1 (PD) \rightarrow l_1t_2 (ND) \rightarrow l_2t_1 (PD) \rightarrow l_2t_2 (ND) and the minimum deformation is 200 μm . The experimental results are in good agreement with the simulation results, and the mean relative error is less than 10%.

Acknowledgments

This research was financially supported by National Natural Science Foundation of China (No. 52275503), the State Key Laboratory of Materials Processing and Die & Mold Technology, Huazhong University of Science and Technology (P2022-018), Key Research and Development Program Project of Hubei Provincial (2022BAD102), Science and Technology Research Project of Department of Education of Hubei Province (B2022026), and the Open Fund of Hubei Key Laboratory of Mechanical Transmission and Manufacturing Engineering at Wuhan University of Science and Technology (MTMEOF2023B05).

References

1. L. Zhu, P. Xue, Q. Lan, G. Meng, Y. Ren, Z. Yang, and Z. Liu, Recent Research and Development Status of Laser Cladding: A Review, *Opt. Laser Technol.*, 2021, **138**, 106915
2. T. Larimian, B. AlMangour, D. Grzesiak, G. Walunj, and T. Borkar, Effect of Laser Spot Size, Scanning Strategy, Scanning Speed, and Laser Power on Microstructure and Mechanical Behavior of 316L Stainless Steel Fabricated via Selective Laser Melting, *J. Mater. Eng. Perform.*, 2022, **31**, p 2205–2224
3. J. Jin, A. Wurikaixi, J. Zhang, and M. Alafate, Research Progress of Thin-wall Parts Formed by Laser Deposition Technology, *Hot. Work. Technol.*, 2017, **46**(10), p 25–29
4. X. Li and Z. Liu, Experimental Study on Scanning Strategy of Laser Cladding Additive Manufacturing Process for Ring-shaped Thin-walled Part, *Tool. Eng.*, 2021, **55**(4), p 24–27
5. Z. Cui, X. Hu, S. Dong, S. Yan, and X. Zhao, Numerical Simulation and Experimental Study on Residual Stress in The Curved Surface Forming of 12CrNi2 Alloy Steel by Laser Melting Deposition, *Materials*, 2020, **13**, p 4316
6. G. Lian, H. Zhang, Y. Zhang, X. Huang, C. Chen, and J. Jiang, Investigation of Geometric Characteristics in Curved Surface Laser Cladding with Curve Path, *Metals-Basel*, 2019, **9**, p 947

7. L. Shu, J. Wang, H. Bai, Y. He, and B. Wang, Numerical and Experimental Investigation on Laser Cladding Treatment of Wear Shaft Surface, *J. Mech. Eng.*, 2019, **55**(9), p 217–223
8. J. Wang, Y. Dai, Y. Hong, and F. Chen, Thermal Analysis of Asperity in Spherical Plain Bearing, *J. Harbin. Inst. Technol.*, 2020, **52**(1), p 8–13
9. B. Song, T. Yu, X. Jiang, L. Chen, W. Xi, and C. Guan, Evolution and Convection Mechanism of The Melt Pool Formed by V-groove Laser Cladding, *Opt. Laser Technol.*, 2021, **144**, 107443
10. Z. Weng, A. Wang, Y. Wang, D. Xiong, and H. Tang, Diode laser cladding of Fe-based alloy on ductile cast iron and related interfacial behavior, *Surf. Coat. Technol.*, 2016, **286**, p 64–71
11. Y. Feng, X. Pang, K. Feng, Y. Feng, and Z. Li, A Method for Evaluating The Crack Resistance and Predicting The Preheating Temperature of High Hardness Coating Prepared by Laser Cladding, *Surf. Coat. Technol.*, 2022, **432**, 128076
12. H. Wang, J. Mo, S. Mu, M. Zhang, W. Duan, J. Li, and Z. Zhou, Effects of Interfacial Trapezoidal Grooves on The Mechanical Properties of Coatings by Laser Cladding, *Surf. Coat. Technol.*, 2021, **421**, 127425
13. J. Wang, J. Zhang, G. Liu, L. Liang, G. Yang, A. Huang, and S. Pang, Effects of Scanning Strategies on Residual Stress and Deformation by High-power Direct Energy Deposition: Island Size and Laser Jump Strategy between Islands, *J. Manuf. Process.*, 2022, **75**, p 23–40
14. Q. Zhi, J. Niu, X. Tan, R. Pei, Y. Liu, Y. Chen, and W. Liu, Effect of Scanning Process and Heat Treatment on Microstructure and Mechanical Property of Inconel 718 Fabricated by Selective Laser Melting, *J. Mater. Eng. Perform.*, 2023, **32**(21), p 9515–9524
15. X. Zhao, S. Dong, S. Yan, X. Liu, Y. Liu, D. Xia, Y. Lv, P. He, B. Xu, and H. Han, The effect of different scanning strategies on microstructural evolution to 24CrNiMo alloy steel during direct laser deposition, *Mater. Sci. Eng. A*, 2020, **771**, 138557
16. D. Patra Karmakar, G. Muvvala, and A.K. Nath, Effect of Scan Strategy and Heat Input on The Shear Strength of Laser Cladded Stellite 21 Layers on AISI H13 Tool Steel in As-deposited and Heat Treated Conditions, *Surf. Coat. Technol.*, 2020, **384**, p 125331
17. G. Li, L. Wang, G. Zhu, L. Zhao, and S. Shi, Influence of Scanning Patterns on Residual Stress of Cladding Layer and Substrate Deformation Produced by Hollow-ring Laser Cladding, *Surf. Technol.*, 2021, **50**(3), p 158–170
18. J. Sun, Y. Zhao, L. Yang, and T. Yu, Process Optimization for Improving Topography Quality and Manufacturing Accuracy of Thin-walled Cylinder Direct Laser Fabrication, *Int. J. Adv. Manuf. Technol.*, 2019, **105**(5–6), p 2087–2101
19. W. Fu, H. Fang, X. Bai, and G. Chen, Effect of Process Paths on Residual Stress of Multi-layer and Multi-pass Laser Cladding, *Trans. China. Weld. Inst.*, 2019, **40**(6), p 29–33
20. S. Huang, S. Qiao, C. Shao, L. Li, S. Li, D. Deng, and F. Lu, Study on Residual Stress Evolution of Laser Cladding Low Chromium Carbon Alloy on Low-pressure Rotor, *J. Manuf. Process.*, 2023, **85**, p 31–42
21. H. Jia, H. Sun, H. Wang, Y. Wu, and H. Wang, Scanning Strategy in Selective Laser Melting (SLM): A Review, *Int. J. Adv. Manuf. Technol.*, 2021, **113**(9–10), p 2413–2435
22. L. Zhu, S. Wang, H. Pan, C. Yuan, and X. Chen, Research on Remanufacturing Strategy for 45 Steel Gear Using H13 Steel Powder Based on Laser Cladding Technology, *J. Manuf. Process.*, 2020, **49**, p 344–354
23. T. Yu, J. Sun, W. Qu, Y. Zhao, and L. Yang, Influences of z-axis Increment and Analyses of Defects of AISI 316L Stainless Steel Hollow Thin-walled Cylinder, *Int. J. Adv. Manuf. Technol.*, 2018, **97**(5–8), p 2203–2220
24. Y. Wu, P. Ma, W. Bai, and J. Chen, Numerical Simulation of Temperature Field and Stress Field in 316L/AISI304 Laser Cladding with Different Scanning Strategies, *Chin. J. Lasers*, 2021, **48**(22), p 12–23
25. J. Xu, Z. Xia, P. Chen, S. Shi, S. Huang, and L. Wang, Modeling of Hollow Ring Laser Heat Source and Finite Element Simulation of Temperature Field, *Chin. J. Lasers*, 2021, **48**(17), p 25–34
26. A. Kumar and M. Shukla, Numerical Modeling of Selective Laser Melting: Influence of Process Parameters on the Melt Pool Geometry, *J. Mater. Eng. Perform.*, 2023, **32**(17), p 7998–8013
27. D. Deng, FEM Prediction of Welding Residual Stress and Distortion in Carbon Steel Considering Phase Transformation Effects, *Mater. Design.*, 2009, **30**(2), p 359–366
28. Q. Zhang, P. Xu, G. Zha, Z. Ouyang, and D. He, Numerical Simulations of Temperature and Stress Field of Fe-Mn-Si-Cr-Ni Shape Memory Alloy Coating Synthesized by Laser Cladding, *Optik*, 2021, **242**, 167079
29. G. Barragan, D.A.R. Perilla, J.G. Nuñez, F. Mariani, and R. Coelho, Correction to: Characterization and Optimization of Process Parameters for Directed Energy Deposition Powder-Fed Laser System, *J. Mater. Eng. Perform.*, 2021, **30**, p 7071
30. S. Wu, Z. Liu, X. Huang, Y. Wu, and Y. Gong, Process Parameter Optimization and EBSD Analysis of Ni60A-25% WC Laser Cladding, *Int. J. Refract. Met. H.*, 2021, **101**, 105675
31. J. Yu, W. Sun, H. Huang, and Y. Huang, Study on the Deformation Control and Microstructures of Thin-Walled Parts Repaired by Laser Cladding, *Coatings*, 2020, **10**(4), p 369
32. L. Xie, W. Shi, T. Wu, M. Gong, J. Huang, Y. Xie, and K. He, Numerical Simulation of Temperature Field and Stress Field of Laser Cladding on Curved Substrate Workpiece, *Surf. Technol.*, 2022, **51**(3), p 296–303

Publisher's Note Springer Nature remains neutral with regard to jurisdictional claims in published maps and institutional affiliations.

Springer Nature or its licensor (e.g. a society or other partner) holds exclusive rights to this article under a publishing agreement with the author(s) or other rightsholder(s); author self-archiving of the accepted manuscript version of this article is solely governed by the terms of such publishing agreement and applicable law.